

1 We appreciate very much of the comments. In the following, the original comments are marked
2 green followed by our reply with no color. Following our response is the full paper with tracked
3 changes.

4
5 Comments to the Author:

6 Page 19, lines 493-494: Author cite Friedlingstein 2019 for the most recent GCB but their
7 summary in these lines misses two source terms of the global carbon budget. Technically I think
8 we would call annual growth in atmospheric CO₂ concentrations the 'net' of sources and sinks,
9 not the 'sum'.

10
11 In the revision, we revised the sentence to “The annual atmospheric CO₂ growth rate, which is
12 the net difference between fossil fuel emissions and total annual sink over land and ocean...”

13
14 Page 20, lines 505-506: Authors change units here (from GtC to %) but they have not quoted
15 GCB correctly. For decade 2009-2018, GCB has ocean sink at 2.5 +/- 0.6 GtC yr⁻¹ and land sink
16 at 3.2 +/- 0.6 GtC yr⁻¹. Land significantly greater than ocean in GCB while these authors have
17 ocean greater than land. Something wrong somewhere. Reader can not accept (line 507) that
18 these numbers fit within uncertainty of GCB numbers.

19 This comment arises from the misunderstanding of the NBE definition. The land sink at 3.2 ± 0.6
20 GtC from GCB does not include land use changes and residual imbalance, while the NBE we
21 report here includes all land fluxes except fossil fuel emissions. We define the term “NBE” in the
22 introduction as: “The net biosphere exchange (NBE), which is the net carbon flux of all the land-
23 atmosphere exchange processes except fossil fuel emissions ...”.

24
25 In section 4.1, we further clarify how we calculate NBE from GCB – 2019 reported fluxes: “The
26 GCB does not report NBE directly, we calculate NBE from GCB-2019 as the residual differences
27 between fossil fuel, ocean net carbon sink, and atmospheric CO₂ growth rate. It is also equivalent
28 to ($S_{\text{LAND}} + B_{\text{IM}} - E_{\text{LUC}}$) reported by Friedlingstein et al., 2019, where S_{LAND} is terrestrial sink, B_{IM}
29 is a budget imbalance, and E_{LUC} is land use change.”

30
31 Authors here refer to GCP (Global Carbon Project?)? Friedlingstein 2019 refers to GCB: global
32 carbon budget. Neither Friedlingstein 2019 nor Friedlingstein 2020 make any mention of NBE.
33 This section (4.1) needs complete rewrite: use correct terms, adopt consistent units (GtC or %) but
34 not both, line 507 conflicts with line 516-517. NBE as defined here does not match terms from
35 GCB. What happened to cement? Do these authors adopt the same +/- 1 sigma as GCB? ESSD
36 readers who might take an interest in this product will very likely know GCB in good detail to
37 detect deficiencies here.

38 See our response above. Even though Friedlingstein et al. (2019, 2020) do not report the term NBE,
39 they calculate ($S_{\text{LAND}} + B_{\text{IM}} - E_{\text{LUC}}$) when comparing to fluxes from top-down atmospheric flux
40 inversions (Figure 8 in Friedlingstein et al. ,2019), which is equivalent to NBE we report here.

41
42 In the revision, we have added the fluxes in GtC in section 4.1. Cement is counted in the fossil
43 fuel emissions.

44
45 In section 2.4, we detailed the uncertainty quantification method.

Line 552 - TER not defined. Not defined until line 712.
TER is defined in the first sentence of section 2.5.1.

Line 733: Authors refer to GCP when they mean GCB. Fix all of these errors! GCP 2019 not a valid citation, Friedlingstein 2019 is.
In the revision, we have removed the GCP and replaced it with GCB-2019.

Line 738 to 746, illogical. Continental US (CONUS) and state-level of CONUS have very good observational data (ground and aircraft). Therefore, observational basis of CO₂ emission for these particular regions (authors do NOT go to state level) will likely always prove more reliable (less uncertain) than satellite xCO₂. Unreliable estimates of NBE, no matter how well distributed over CONUS, will never prove more reliable than obs here. But validation here can add credibility to xCO₂ inversions elsewhere? Authors current paragraph implies that because NBE varies a lot regionally or seasonally, it will prove useful here. Not likely. 1.5 C target (hopeful) comes from UNFCCC Cop21 Paris Agreement, not from IPCC AR6. IPCC AR6 never cited here.

What we want to convey in that paragraph is that it is important to monitor the changes of NBE since the regional contributions to atmospheric CO₂ growth rate is the sum of NBE and fossil fuel emissions. It seems that the US example generates confusion. In the revision, we deleted the sentence: “Even over the continental US, where fossil fuel emissions are ~1.5 GtC/year, the changes of regional NBE in the future can significantly modify regional contributions to the changes of atmospheric CO₂ (Liu et al., 2018).”

The 1.5 C target is discussed in IPCC special report, 2018. We revised the citation in the revision.

Supplement consists entirely of figures, with some redundancy to main text. Because Copernicus does not archive supplements, this supplement needs to go on the JPL site or these 11 figures need to go in the Appendix.

I am perplexed here, since I do see ESSD papers with supplement materials published online. Here are a few examples:

Yu, Q., You, L., Wood-Sichra, U., Ru, Y., Joglekar, A. K. B., Fritz, S., Xiong, W., Lu, M., Wu, W., and Yang, P.: A cultivated planet in 2010 – Part 2: The global gridded agricultural-production maps, *Earth Syst. Sci. Data*, 12, 3545–3572, <https://doi.org/10.5194/essd-12-3545-2020>, 2020.

McDuffie, E. E., Smith, S. J., O'Rourke, P., Tibrewal, K., Venkataraman, C., Marais, E. A., Zheng, B., Crippa, M., Brauer, M., and Martin, R. V.: A global anthropogenic emission inventory of atmospheric pollutants from sector- and fuel-specific sources (1970–2017): an application of the Community Emissions Data System (CEDS), *Earth Syst. Sci. Data*, 12, 3413–3442, <https://doi.org/10.5194/essd-12-3413-2020>, 2020.

If it is still possible, we prefer to have supplement instead of having figures in the Appendix. But to accelerate the publication of the paper, in the revision, we have put the supplement figures in the Appendix B.

Carbon Monitoring System Flux Net Biosphere Exchange 2020 (CMS-Flux NBE 2020)

Junjie Liu^{1,2*}, Latha Baskaran¹, Kevin Bowman¹, David S. Schimel¹, A. Anthony Bloom¹, Nicholas C. Parazoo¹, Tomohiro Oda^{3,4}, Dustin Carroll⁵, Dimitris Menemenlis¹, Joanna Joiner⁶, Roisin Commance⁷, Bruce Daube⁸, Lucianna V. Gatti⁹, Kathryn McKain^{10,11}, John Miller¹⁰, Britton B. Stephens¹², Colm Sweeney¹⁰, Steven Wofsy⁸,

1. Jet Propulsion Laboratory, Caltech, CA
2. Caltech, CA
3. Global Modeling and Assimilation Office, NASA Goddard Space Flight Center
4. Goddard Earth Sciences Technology and Research, Universities Space Research Association, Columbia, MD
5. Moss Landing Marine Laboratories, San José State University, California, CA
6. Laboratory for Atmospheric Chemistry and Dynamics, NASA Goddard Space Flight Center
7. Lamont-Doherty Earth Observatory of Columbia University, NY
8. Harvard University, Cambridge, MA
9. LaGEE, CCST, INPE- National Institute for Space Research, Brazil
10. NOAA, Global Monitoring Laboratory, Boulder, CO 80305
11. University of Colorado, Cooperative Institute for Research in Environmental Sciences, Boulder, CO
11. National Center for Atmospheric Research, Boulder, CO 80301

Correspondence: Junjie Liu (junjie.liu@jpl.nasa.gov)

Abstract. Here we present a global and regionally-resolved terrestrial net biosphere exchange (NBE) dataset with corresponding uncertainties between 2010–2018: CMS-Flux NBE 2020. It is estimated using the NASA Carbon Monitoring System Flux (CMS-Flux) top-down flux inversion system that assimilates column CO₂ observations from the Greenhouse gases Observing SATellite (GOSAT) and NASA’s Observing Carbon Observatory -2 (OCO-2). The regional monthly fluxes are readily accessible as tabular files, and the gridded fluxes are available in NetCDF format. The fluxes and their uncertainties are evaluated by extensively comparing the posterior CO₂ mole fractions with CO₂ observations from aircraft and the NOAA marine boundary layer reference sites. We describe the characteristics of the dataset as global total, regional climatological mean, and regional annual fluxes and seasonal cycles. We find that the global total fluxes of the dataset agree with atmospheric CO₂ growth observed by the surface-observation network within uncertainty. Averaged between 2010 and 2018, the tropical regions range from close-to neutral in tropical South America to a net source in Africa; these contrast with the extra-tropics, which are a net sink of 2.5 ± 0.3 gigaton carbon per year. The regional satellite-constrained NBE estimates provide a unique perspective for understanding the terrestrial biosphere carbon dynamics and monitoring changes in regional contributions to the changes of atmospheric CO₂ growth rate. The gridded and regional aggregated dataset can be accessed at: <https://doi.org/10.25966/4v02-c391> (Liu et al., 2020).

1 Introduction

New “top-down” inversion frameworks that harness satellite observations provide an important complement to global aggregated fluxes (e.g., Global Carbon Budget (GCB), Friedlingstein et al., 2019) and inversions based on surface CO₂ observations (e.g., Chevallier et al., 2010), especially over the tropics and the Southern Hemisphere (SH) where conventional surface CO₂ observations are sparse. The net biosphere exchange (NBE), which is the net carbon flux of all the land-atmosphere exchange processes except fossil fuel emissions, is far more variable and uncertainty than ocean fluxes (Lovenduski and Bonan, 2017) or fossil fuel emissions (Yin et al, 2019), and is thus the focus of this dataset estimated from a top-down atmospheric CO₂ inversion of satellite column CO₂ dry-air mole fraction (X_{CO_2}). Here, we present the global and regional NBE as a series of maps, time series and tables, and disseminate it as a public dataset for further analysis and comparison to other sources of flux information. The gridded NBE dataset and its uncertainty, air-sea fluxes, and fossil fuel emissions are also available, so that users can calculate carbon budget from regional to global scale. Finally, we provide a comprehensive evaluation of both mean and uncertainty estimates against the CO₂ observations from independent airborne datasets and the NOAA marine boundary layer (MBL) reference sites (Conway et al., 1994).

Global top-down atmospheric CO₂ flux inversions have been historically used to estimate regional terrestrial NBE. They make uses of the spatiotemporal variability of atmospheric CO₂, which is dominated by NBE, to infer net carbon exchange at the surface (Chevallier et al., 2005; Baker et al., 2006; Liu et al., 2014). The accuracy of the NBE from top-down flux inversions is determined

Deleted: Project

Deleted: , which is the net carbon flux of all the land-atmosphere exchange processes except fossil fuel emissions

by the density and accuracy of the CO₂ observations, the accuracy of modeled atmospheric transport, and knowledge of the prior uncertainties of the flux inventories.

For CO₂ flux inversions based on high precision *in situ* and flask observations, the measurement error is low (<0.2 parts per million (ppm)) and not a significant source of error; however, these observations are limited spatially, and are concentrating primarily over North America (NA) and Europe (Crowell et al., 2019). Satellite X_{CO₂} from CO₂-dedicated satellites, such as the Greenhouse Gases Observing Satellite (GOSAT) (launched in July 2009) and the Observing Carbon Observatory 2 (OCO-2) (Crisp et al., 2017) have much broader spatial coverage (O'Dell et al., 2018), which fill the observational gaps of conventional surface CO₂ observations, but they have up to an order of magnitude higher single-sounding uncertainty and potential systematic errors compared to the *in situ* and flask CO₂ observations. Recent progress in instrument error characterization, spectroscopy, and retrieval methods have significantly improved the accuracy and precision of the X_{CO₂} retrievals (O'Dell et al., 2018; Kiel et al., 2019). The single sounding random error of X_{CO₂} from OCO-2 is ~1.0 ppm (Kulawik et al., 2019). A recent study by Byrne et al. (2020) shows less than a 0.5 ppm difference between posterior X_{CO₂} constrained by a recent data set, ACOS-GOSAT b7 X_{CO₂} retrievals, and those constrained by conventional surface CO₂ observations. Chevallier et al. (2019) also showed that an OCO-2 based flux inversion had similar performance to surface CO₂ based flux inversions when comparing posterior CO₂ mole fractions to aircraft CO₂ in the free troposphere. Results from these studies show that systematic uncertainties in CO₂ retrievals from satellites are comparable to, or smaller than, other uncertainty sources in atmospheric inversions (e.g. transport).

189 A newly-developed biogeochemical model-data fusion system, CARDAMOM, made progress in
190 producing NBE uncertainties, along with mean values that are consistent with a variety of
191 observations assimilated through a Markov Chain Monte Carlo (MCMC) method (Bloom et al.,
192 2016; 2020). Transport model errors in general have also been reduced relative to earlier transport
193 model intercomparison efforts, such as TransCom 3 (Gurney et al., 2004; Gaubert et al., 2019).
194 Advancements in satellite retrieval, transport, and prior terrestrial biosphere modeling have led to
195 more mature inversions constrained by satellite X_{CO_2} observations.

196
197 Two satellites, GOSAT and OCO-2, have now produced more than 10 years of observations. Here
198 we harness the CMS-Flux inversion framework (Liu et al., 2014; 2017; 2018; Bowman et al., 2017)
199 to generate an NBE product: CMS-Flux NBE 2020, by assimilating both GOSAT and OCO-2 from
200 2010–2018. The dataset is the longest satellite-constrained NBE product so far. The CMS-Flux
201 framework exploits globally available X_{CO_2} to infer spatially-resolved total surface-atmosphere
202 exchange. In combination with constituent fluxes, e.g., Gross Primary Production (GPP), NBE
203 from CMS-Flux framework have been used to assess the impacts of El Niño on terrestrial
204 biosphere fluxes (Bowman et al, 2017; Liu et al, 2017) and the role of droughts in the North
205 American carbon balance (Liu et al, 2018). These fluxes have furthermore been ingested into land-
206 surface data assimilation systems to quantify heterotrophic respiration (Konings et al., 2019),
207 evaluate structural and parametric uncertainty in carbon-climate models (Quetin et al., 2020), and
208 inform climate dynamics (Bloom et al., 2020). We present the regional NBE and its uncertainty
209 based on three types of regional masks: (1) latitude and continent, 2) distribution of biome types
210 (defined by plant functional types) and continent, and 3) TransCom regions (Gurney et al., 2004).

211

212 The outline of the paper is as follows: Section 2 describes methods, and Sections 3 and 4 describe
 213 the dataset and the major NBE characteristics, respectively. We extensively evaluate the posterior
 214 fluxes and uncertainties by comparing the posterior CO₂ mole fractions against aircraft
 215 observations and the NOAA MBL reference CO₂, and a gross primary production (GPP) product
 216 (section 5). In Section 6, we discuss the strength and weakness, and potential usage of the data. A
 217 summary is provided in Section 7, and Section 8 describes the dataset availability and future plan.

219 2 Methods

220 2.1 CMS-Flux inversion system

221 The CMS-Flux framework is summarized in Figure 1. The center of the system is the CMS-Flux
 222 inversion system, which optimizes NBE and air-sea net carbon exchanges with a 4D-Var inversion
 223 system (Liu et al., 2014). In the current system, we assume no uncertainty in fossil fuel emissions,
 224 which is a widely adopted assumption in global flux inversion systems (e.g., Crowell et al., 2019),
 225 since the uncertainty in fossil fuel emissions at regional scales is substantially less than the NBE
 226 uncertainties. The 4D-Var minimizes a cost function that includes two terms:

$$227 \quad J(\mathbf{x}) = (\mathbf{x} - \mathbf{x}_b)^T \mathbf{B}^{-1} (\mathbf{x} - \mathbf{x}_b) + (\mathbf{y} - h(\mathbf{x}))^T \mathbf{R}^{-1} (\mathbf{y} - h(\mathbf{x})) \quad (1)$$

228 The first term measures the differences between the optimized fluxes and the prior fluxes
 229 normalized by the prior flux error covariance \mathbf{B} . The second term measures the differences between
 230 observations (\mathbf{y}) and the corresponding model simulations ($h(\mathbf{x})$) normalized by the observation
 231 error covariance \mathbf{R} . The term $h(\cdot)$ is the observation operator that calculates observation-
 232 equivalent model-simulated X_{CO₂}. The 4D-Var uses the adjoint (i.e., the backward integration of
 233 the transport model) (Henze et al., 2004) of the GEOS-Chem transport model to calculate the
 234 sensitivity of the observations to surface fluxes. The configurations of the inversion system are

Field Code Changed

Field Code Changed

Field Code Changed

summarized in Table 1. We run both the forward and adjoint at $4^\circ \times 5^\circ$ spatial resolution, and optimize monthly NBE and air-sea carbon fluxes at each grid point from January 2010 to December 2018. Inputs for the system include prior carbon fluxes, meteorological drivers, and the satellite X_{CO_2} (Figure 1). Section 2.2 (Table 2) describes the prior flux and its uncertainties, and section 2.3 (Table 3) describes the observations and the corresponding uncertainties.

2.2 The prior CO_2 fluxes and uncertainties

The prior CO_2 fluxes include NBE, air-sea carbon exchange, and fossil fuel emissions (see Table 2). The data sources for the prior fluxes are listed in Table 7 and provided in the gridded fluxes. Methods to generate prior ocean carbon fluxes and fossil fuel emissions are documented in Brix et al., (2015), Carroll et al. (2020), and Oda et al. (2018). The focus of this dataset is optimized terrestrial biosphere fluxes, so we briefly describe the prior terrestrial biosphere fluxes and their uncertainties.

We construct the NBE prior using the CARDAMOM framework (Bloom et al., 2016). The CARDAMOM data assimilation system explicitly represents the time-resolved uncertainties in the NBE. The prior estimates are already constrained with multiple data streams accounting for measurement uncertainties following a Bayesian approach similar to that used in the 4D-variational approach. We use the CARDAMOM setup as described by Bloom et al. (2016, 2020) resolved at monthly timescales; data constraints include GOME-2 solar-induced fluorescence (Joiner et al., 2013), MODIS Leaf Area Index (LAI), and biomass and soil carbon (details on the data assimilation are provided in Bloom et al. (2020)). In addition, mean GPP and fire carbon emissions from 2010 - 2017 are constrained by FLUXCOM RS+METEO version 1 GPP

258 (Tramontana et al., 2016; Jung et al., 2017) and GFEDv4.1s (Randerson et al., 2018), respectively,
259 both assimilated with an uncertainty of 20%. We use the Olsen and Randerson (2001) approach to
260 downscale monthly GPP and respiration fluxes to 3-hourly timescales, based on ERA-interim re-
261 analysis of global radiation and surface temperature. Fire fluxes are downscaled using the
262 GFEDv4.1 daily and diurnal scale factors on monthly emissions (Giglio et al., 2013).
263 Posterior CARDAMOM NBE estimates are then summarized as NBE mean and standard
264 deviation values.

265

266 The NBE from CARDAMOM shows net carbon uptake of 2.3 GtC/year over the tropics and close
267 to neutral in the extratropics (Figure B1). The year-to-year variability (i.e., interannual variability,
268 IAV) estimated from CARDAMOM from 2010–2017 is generally less than 0.1 gC/m²/day outside
269 of the tropics (Figure B1). Because of the weak interannual variability estimated by CARDAMOM,
270 we use the same 2017 NBE prior for 2018.

271

272 CARDAMOM generates uncertainty along with the mean state. The relative uncertainty over the
273 tropics is generally larger than 100%, and the magnitude is between 50% and 100% over the extra-
274 tropics (Figure B2). We assume no correlation in the prior flux errors in either space or time. The
275 temporal and spatial error correlation estimates can in principle be computed by CARDAMOM.
276 We anticipate incorporating these error correlations in subsequent versions of this dataset.

277

278 2.3 Column CO₂ observations from GOSAT and OCO-2

279 We use the satellite-column CO₂ retrievals from Atmospheric Carbon Observations from Space
280 (ACOS) team for both GOSAT (version 7.3) and OCO-2 (version 9) (Table 3). The use of the
281 same retrieval algorithm and validation strategy adopted by the ACOS team to process both

Deleted: S1

Deleted: S1

Deleted: S2

285 GOSAT and OCO-2 spectra maximizes the consistency between these two datasets. Both GOSAT
286 and OCO-2 satellites carry high-resolution spectrometers optimized to return high precision
287 measurements of reflected sunlight within CO₂ and O₂ absorption bands in the shortwave infrared
288 (Crisp et al., 2012). Both satellites fly in a sun-synchronous orbit. GOSAT has a $13:00 \pm 0.15$
289 hours local passing time and a three-day ground track repeat cycle. The footprint of GOSAT is
290 ~ 10.5 km in diameter in sun-nadir view (Crisp et al., 2012). The daily number of soundings
291 processed by the ACOS-GOSAT retrieval algorithm is between a few hundreds to ~ 2000 . Further
292 quality control and filtering reduce the ACOS-GOSAT X_{CO₂} retrievals to $\sim 100 - 300$ daily (Figure
293 [B5](#) in Liu et al., 2017). We only assimilate ACOS-GOSAT land nadir observations flagged as
294 being good quality, which are the retrievals with quality flag equal to zero.

Deleted: S5

295
296 OCO-2 has a 13:30 local passing time and 16-day ground track repeat cycle. The nominal
297 footprints of the OCO-2 are 1.25 km wide and ~ 2.4 km along the orbit. Because of their small
298 footprints and sampling strategy, OCO-2 has many more X_{CO₂} retrievals than ACOS-GOSAT. To
299 reduce the sampling error due to the resolution differences between the transport model and OCO-
300 2 observations, we generate super observations by aggregating the observations within ~ 100 km
301 (along the same orbit) (Liu et al., 2017). The super-obsing strategy was first proposed in numerical
302 weather prediction (NWP) to assimilate dense observations (Lorenc, 1981), and is still broadly
303 used in NWP (e.g., Liu and Rabier, 2003). More detailed information about OCO-2 super
304 observations can be found in Liu et al. (2017). OCO-2 has four observing modes: land nadir, land
305 glint, ocean glint, and target. Following Liu et al. (2017), we only use land nadir observations. The
306 super observations have more uniform spatial coverage and are more comparable to the spatial

representation of ACOS-GOSAT observations and the transport model (see Figure B5 in Liu et al., 2017).

Deleted: S5

We directly use observational uncertainty provided with ACOS-GOSAT b7.3 to represent the observation error statistics, \mathbf{R} , in Eq 1. The uncertainty of the OCO-2 super observations is the sum of the variability of X_{CO_2} used to generate each individual super observation and the mean uncertainty provided in the original OCO-2 retrievals. Kulawik et al. (2019) showed that both OCO-2 and ACOS-GOSAT bias-corrected retrievals have a mean bias of -0.1 ppm when compared with X_{CO_2} from Total Carbon Column Observing Network (TCCON) (Wunch et al., 2011), indicating consistency between ACOS-GOSAT and OCO-2 retrievals. O'Dell et al. (2018) showed that the OCO-2 X_{CO_2} land nadir retrievals has RMS error of ~1.1 ppm when compared to TCCON retrievals; the differences between OCO-2 X_{CO_2} retrievals and surface CO_2 constrained model simulations are well within 1.0 ppm over most of the locations in the Northern Hemisphere (NH), where most of the surface CO_2 observations are located.

The magnitude of observation errors used in \mathbf{R} is generally above 1.0 ppm, larger than the sum of random error and biases in the observations. The ACOS-GOSAT b7.3 observations from July 2009–June 2015 are used to optimize fluxes between 2010 and 2014, and the OCO-2 X_{CO_2} observations from Sep 2014–June 2019 are used to optimize fluxes between 2015 and 2018.

The observational coverage of ACOS-GOSAT and OCO-2 is spatiotemporally dependent, with more coverage during summer than winter over the NH, and more observations over mid-latitudes than over the tropics (Figure B3). The variability (i.e., standard deviation) of annual total number

Deleted: S3

of observations from 2010–2014 is within 4% of the annual mean number for ACOS-GOSAT. Except for a data gap in 2017 caused by a malfunction of the OCO-2 instrument, the variability of the annual total number of observations between 2015 and 2018 is within 8% of the annual mean number for OCO-2.

2.4 Uncertainty quantification

The posterior flux error covariance is the inverse Hessian, which incorporates the transport, measurement, and background errors at the 4D-Var solution (Eq. 13 in Bowman et al, 2017). Posterior flux uncertainty projected to regions can be estimated analytically based on the methods described in Fisher and Courtier (1995) and Meirink et al. (2008), using either flux singular vectors or flux increments obtained during the iterative optimization (e.g., Niwa and Fujii, 2020). In this study, we rely on a Monte Carlo approach to quantify posterior flux uncertainties following Chevallier et al. (2010) and Liu et al. (2014), which is simpler and widely used. In this approach, an ensemble of flux inversions is carried out with an ensemble of priors and simulated observations to sample the uncertainties of prior fluxes (i.e., \mathbf{B} in eq. 1) and observations (\mathbf{R} in Eq. 1), respectively. The magnitude of posterior flux uncertainties is a function of assumed uncertainties in prior fluxes and observations, as well as the density of observations. Since the density of GOSAT and OCO-2 observations are stable (section 2.3) within their respective data record, we characterize the posterior flux uncertainties for 2010 and 2015 only, and assume the flux uncertainties for 2011–2014 are the same as 2010 and flux uncertainties for 2016–2018 are the same as 2015.

2.5 Evaluation of posterior fluxes

356 Direct NBE estimates from flux towers only provide a spatial representation of roughly 1 – 3
357 kilometers (Running et al., 1999), not appropriate to evaluate regional NBE from top-down flux
358 inversions. Thus, we use two methods to indirectly evaluate the posterior NBE and its uncertainties.
359 One is to compare annual NBE anomalies and seasonal cycle to a gross primary production (GPP)
360 product. The other is to compare posterior CO₂ mole fractions to independent (i.e., not assimilated
361 in the inversion) aircraft and the NOAA MBL reference observations. The second method has been
362 broadly used to indirectly evaluate posterior fluxes from top-down flux inversions (e.g., Stephens
363 et al., 2007; Liu and Bowman, 2016; Chevallier et al., 2019; Crowell et al., 2019). In addition to
364 these two methods, we also compare the NBE seasonal cycles to three publicly available top-down
365 NBE estimates that are constrained by surface CO₂ observations (Tables 3 and 7).

366 **2.5.1 Evaluation against independent gross primary production (GPP) product**

367 NBE is a small residual difference between two large terms: total ecosystem respiration (TER)
368 and GPP, plus fire. A positive NBE anomaly (i.e., less uptake from the atmosphere) has been
369 shown to correspond to reduced GPP caused by climate anomalies (e.g., Bastos et al., 2018), and
370 the magnitude of net uptake is proportional to GPP in most biomes observed by flux tower
371 observations (e.g., Falk et al., 2008). Since NBE is related not only to GPP, the comparison to GPP
372 only serves as a qualitative measure of the NBE quality. For example, we would expect that the
373 posterior NBE seasonality to be anti-correlated with GPP in the temperate and high latitudes. In
374 this study, we use FLUXSAT GPP (Joiner et al., 2018), which is an upscaled GPP product based
375 on flux tower GPP observations and satellite-based geometry adjusted reflectance from the
376 MODerate-resolution Imaging Spectroradiometer (MODIS) and solar-induced chlorophyll
377 fluorescence observations from Global Ozone Monitoring Experiment – 2 (GOME-2) (Joiner et

al., 2013). Joiner et al. (2018) show that the agreement between FLUXSAT-GPP and GPP from flux towers is better than other available upscaled GPP products.

2.5.2 Evaluation against aircraft and the NOAA marine boundary layer (MBL) reference CO₂ observations

The aircraft observations used in this study include those published in OCO-2 MIP ObsPack August 2019 (CarbonTracker team, 2019), which include regular vertical profiles from flask samples collected on light aircraft by NOAA (Sweeney et al., 2015) and other laboratories, regular (two to four weekly) vertical profiles from the Instituto de Pesquisas Espaciais (INPE) over tropical South America (SA) (Gatti et al., 2014), and from the Atmospheric Tomography (ATom, Wofsy et al., 2018), HIAPER Pole-to-Pole (HIPPO, Wofsy et al., 2011), the O₂/N₂ Ratio and CO₂ airborne Southern Ocean Study (ORCAS) (Stephens et al., 2017), and [Atmospheric Carbon and Transport - America \(ACT-America, Davis et al., 2018\)](#) aircraft campaigns (Table 3). Figure 2 shows the aircraft observation coverage and density between 2010 and 2018. Most of the aircraft observations are concentrated over NA. ATom had four (1–4) campaigns between August 2016 to May 2018, spanning four seasons over the Pacific and Atlantic Ocean. HIPPO had five (1–5) campaigns over the Pacific, but only HIPPO 3–5 occurred between 2010 and 2011. HIPPO 1–2 occurred in 2009. Based on the spatial distribution of aircraft observations, we divide the comparison into nine regions: Alaska, mid-latitude NA, Europe, East Asia, South Asia, Africa, Australia, Southern Ocean, and South America (Table 4 and Figure 2).

We calculate several quantities to evaluate the posterior fluxes and their uncertainty with aircraft observations. One is the monthly mean differences between posterior and aircraft CO₂ mole

Deleted: and

fractions. The second is the monthly root mean square errors (RMSE) over each of nine sub-regions, which is defined as:

$$RMSE = \left(\frac{1}{n} \sum_{i=1}^n (y_{aircraft}^o - y_{aircraft}^b)^2 \right)^{\frac{1}{2}} \quad (2)$$

where $y_{aircraft}^o$ is the i^{th} aircraft observation, $y_{aircraft}^b$ is the corresponding posterior CO₂ mole fraction sampled at the i^{th} aircraft location, and n is the number of aircraft observations over each region. The RMSE is computed over the n aircraft observations within one of the nine sub-regions. The mean differences indicate the magnitude of the mean posterior CO₂ bias, while the RMSE includes both random and systematic errors in posterior CO₂. The bias and RMSE could be due to errors in posterior fluxes, transport, and initial CO₂ concentrations. When errors in transport and initial CO₂ concentrations are smaller than the errors in the posterior fluxes, the magnitude of biases and *RMSE* indicates the accuracy of the posterior fluxes.

To evaluate the magnitude of posterior flux uncertainty estimates, we compare *RMSE* against the standard deviation of ensemble simulated aircraft observations (equation 3) from the Monte Carlo method (*RMSE_{MC}*). The quantity *RMSE_{MC}* can be written as:

$$RMSE_{MC} = \left[\frac{1}{n_{ens}} \sum_{iens=1}^{n_{ens}} ((y_{aircraft}^{b(MC)})_{iens} - \bar{y}_{aircraft}^{b(MC)})^2 \right]^{\frac{1}{2}} \quad (3)$$

The variable $(y_{aircraft}^{b(MC)})_{iens}$ is the i^{th} ensemble member of simulated aircraft observations from Monte Carlo ensemble simulations, $\bar{y}_{aircraft}^{b(MC)}$ is the mean, and n_{ens} is the total number of ensemble members. For simplicity, in equation (3), we drop the indices for the aircraft observations used in equation (2). In the absence of errors in transport and initial CO₂ concentrations, when the estimated posterior flux uncertainty reflects the “true” posterior flux uncertainty, we show in the Appendix that:

Field Code Changed

423 $RMSE^2 = \frac{1}{n} \sum_{i=1}^n R_{i,i} + RMSE_{MC}^2 \quad (4)$

424 where $R_{aircraft}$ is the aircraft observation error variance, which could be neglected on regional
425 scale.

426

427 We further calculate the ratio r between $RMSE$ and $RMSE_{MC}$:

428 $r = \frac{RMSE}{RMSE_{MC}} \quad (5)$

429 A ratio close to one indicates that the posterior flux uncertainty reflects the true uncertainty in the
430 posterior fluxes when the transport errors are small.

431

432 The presence of transport errors will make the comparison between $RMSE$ and $RMSE_{MC}$
433 potentially difficult to interpret. Even when $RMSE_{MC}$ represents the actual uncertainty in posterior
434 fluxes, the $RMSE$ could be larger than $RMSE_{MC}$, since the differences between aircraft
435 observations and model simulated posterior mole fractions $RMSE$ could be due to errors in both
436 transport and the posterior fluxes, while $RMSE_{MC}$ only reflects the impact of posterior flux
437 uncertainty on simulated aircraft observations. In this study, we assume the primary sources of
438 $RMSE$ come from errors in posterior fluxes.

439

440 The $RMSE$ and $RMSE_{MC}$ comparison only shows differences in CO₂ space. We further calculate
441 the sensitivity of the $RMSE$ to the posterior flux using the GEOS-Chem adjoint. We first define a
442 cost function J as:

443 $J = RMSE^2 \quad (6)$

444 The sensitivity of the mean-square error to a flux, x , at location i and month j is

445 $w_{i,j} = \frac{\partial J}{\partial x_{i,j}} \times x_{i,j} \quad (7)$

446 This sensitivity is normalized by the flux magnitude. Equation 7 can be interpreted as the
 447 sensitivity of the $RMSE^2$ to a fractional change in the fluxes. We can estimate the time-integrated
 448 magnitude of the sensitivity over the entire assimilation window by calculating:

449 $S_i = \frac{\sum_{j=1}^M |w_{i,j}|}{\sum_{k=1}^P \sum_{j=1}^M |w_{k,j}|} \quad (8)$

450 where P is the total number of grid points and M is the total number of months from the time of
 451 the aircraft data to the beginning of the inversion. The numerator of equation (8) quantifies the
 452 absolute total sensitivity of the $RMSE^2$ to the fluxes at the i^{th} grid. Normalized by the total absolute
 453 sensitivity across the globe, the quantity S_i indicates the relative sensitivity of $RMSE^2$ to fluxes at
 454 the i^{th} grid point. Note that S_i is unitless, and it only quantifies sensitivity, not the contribution of
 455 fluxes at each grid to $RMSE^2$.

456

457 We use the NOAA MBL reference dataset (Table 7) to evaluate the CO_2 seasonal cycle over four
 458 latitude bands: 90°N-60°N, 60°N-20°N, 20°N-20°S, and 20°S-90°S. The MBL reference is based
 459 on a subset of sites from the NOAA Cooperative Global Air Sampling Network. Only
 460 measurements that are representative of a large volume air over a broad region are considered. In
 461 the comparison, we first remove the global mean CO_2
 462 (<https://www.esrl.noaa.gov/gmd/ccgg/trends/global.html>) from both the NOAA MBL reference
 463 and the posterior CO_2 .

464

465 **2.6 Regional masks**

We provide posterior NBE from 2010 – 2018 using three sets of regional masks (Figure 3), in addition to the gridded product. The regional mask in Figure 3A is based on a combination of seven plant function types condensed from MODIS IGBP and the TransCom -3 regions (Gurney et al., 2004), which is referred as Region Mask 1 (RM1) in later description. There are 28 regions in Figure 3A: six in NA, four in SA, five in Eurasia (north of 40°N), three in tropical Asia, three in Australia, and seven in Africa. The regional mask in Figure 3B is based on latitude and continents with 13 regions in total, which is referred as Region Mask 2 (RM2) in later description. Figure 3C is the TransCom regional mask with 11 regions on land.

3 Dataset description

We present the fluxes as globally, latitudinally, and regionally aggregated time series. We show the nine-year average fluxes aggregated into RM1, RM2, and TransCom regions (Figure 3). The aggregations are geographic (latitude and continent) and bio-climatic (biome by continent). For each region in the geographic and biome aggregations, we show nine-year mean annual net fluxes and uncertainties, and then the annual fluxes for each region as a set of time-series plots. The month-by-month fluxes and uncertainties are available in tabular format, so the actual aggregated fluxes may be readily compared to bottom-up extrapolated fluxes and Earth System models. Users can also aggregate the gridded fluxes and uncertainties based on their own defined regional masks. Table 5 provides a complete list of all data products available in the dataset. In section 4, we describe the major characteristics of the dataset.

4 Characteristics of the dataset

4.1 Global fluxes

489 The annual atmospheric CO₂ growth rate, which is the ~~net difference between~~ fossil fuel emissions
 490 and total annual sink over land and ocean, is well-observed by the NOAA surface CO₂ observing
 491 network (<https://www.esrl.noaa.gov/gmd/ccgg/ggrn.php>). We compare the global total flux estimates
 492 constrained by GOSAT and OCO-2 with the NOAA CO₂ growth rate from 2010–2018, and discuss
 493 the mean carbon sink over land and ocean. Over these nine years, the satellite-constrained
 494 atmospheric CO₂ growth rate agrees with the NOAA observed CO₂ growth rate within the
 495 uncertainty of the posterior fluxes (Figure 4). The mean annual global surface CO₂ fluxes (in Gt
 496 C/yr) are derived from the NOAA observed CO₂ growth rate (in ppm/yr) using a conversion factor
 497 of 2.124 GtC/ppm (Le Quéré et al., 2018). The estimated growth rate has the largest discrepancy
 498 with the NOAA observed growth rate in 2014, which may be due to a failure of one of the two
 499 solar paddles of GOSAT in May 2014 (Kuze et al., 2016). Over the nine years, the estimated total
 500 accumulated carbon in the atmosphere is 41.5 ± 2.4 GtC, which is slightly lower than the
 501 accumulated carbon based on the NOAA CO₂ growth rate (45.2 ± 0.4 GtC). On average, ~~we~~
 502 ~~estimate that the~~ ~~NBE is 2.0 ± 0.7 GtC, $\sim 20 \pm 8\%$ of fossil fuel emissions, and the ocean sink is~~
 503 ~~3.0 ± 0.1 GtC, $\sim 30 \pm 1\%$ of fossil fuel emissions (Figure 4). These numbers are within the ranges~~
 504 of the corresponding ~~GCB~~ estimates from Freidlingstein et al., 2019 (~~referred as GCB-2019~~
 505 ~~hereafter~~). The mean NBE and ocean sink from ~~GCB-2019~~ are 2.0 ± 1.0 GtC and 2.5 ± 0.5 GtC
 506 ~~respectively, which are $21 \pm 10\%$ and $26 \pm 5\%$ of fossil fuel emissions respectively between 2010–~~
 507 2018. ~~The GCB does not report NBE directly, we calculate~~ ~~NBE from GCB-2019~~ as the residual
 508 differences between fossil fuel, ocean ~~net carbon sink~~, and atmospheric CO₂ growth rate. ~~It~~ is also
 509 equivalent to ~~($S_{\text{LAND}} + B_{\text{IM}} - E_{\text{LUC}}$) reported by Freidlingstein et al., 2019, where S_{LAND} is terrestrial~~
 510 ~~sink, B_{IM} is a budget imbalance, and E_{LUC} is land use change.~~ Over these nine years, we estimate
 511 that ~~NBE ranges from 3.6 GtC ($\sim 37\%$ of fossil fuel emissions) in 2011 (a La Niña year), to only~~

Deleted: sum

Deleted: of

Deleted: land sink

Deleted: is

Deleted: GCP 2019 (

Deleted:)

Deleted: GCP 2019

Deleted: (~ 1.0 GtC estimated residual NBE uncertainty)

Deleted: (~ 0.5 GtC estimated ocean flux uncertainty)

Deleted: The GCP

Deleted: here is calculated

Deleted: fluxe

Deleted: s

Deleted: , and

Deleted: it

Deleted: the sum of carbon fluxes from land use changes, land sink, and residual balance reported by GCP.

Formatted: Subscript

Formatted: Subscript

Deleted: the land sink

Deleted: 37% of fossil fuel emissions

Deleted:

532 0.5 GtC, (~5% of fossil fuel emissions) in 2015 (an El Niño year), consistent with 3.3 GtC (35%
533 of fossil fuel) in 2011 to 0.9 GtC (7% of fossil fuel) in 2015, estimated from GCB-2019. We
534 estimate that the ocean sinks range from 3.5 GtC in 2015 to 2.3 GtC in 2012, larger than the
535 estimated ocean flux ranges of 2.7 in 2016 to 2.5 in 2012 reported by Freidlingstein et al. (2019).

536 4.2 Mean regional fluxes and uncertainties

537 Figure 5 shows the nine-year mean regional annual fluxes, uncertainty, and its variability between
538 2010–2018. Table 6 shows an example of the dataset corresponding to Figure 5 A, D, and G. It
539 shows that large net carbon uptake occurs over Eurasia, NA, and the Southern Hemisphere (SH)
540 mid-latitudes. The largest net carbon uptake is over the eastern US (-0.4 ± 0.1 GtC (1σ uncertainty))
541 and high latitude Eurasia (-0.5 ± 0.1 GtC) (Figure 5A, B). We estimate a net land carbon sink of
542 2.5 ± 0.3 GtC/year between 2010–2013 over the NH mid to high latitudes, which agrees with 2.4
543 ± 0.6 GtC estimates over the same time periods based on a two-box model (Ciais et al., 2019). Net
544 uptake in the tropics ranges from close-to-neutral in tropical South America (0.1 ± 0.1 GtC) to a
545 net source in northern Africa (0.6 ± 0.2 GtC) (Figure 5A, B). The tropics exhibit both large
546 uncertainty and large variability. The NBE interannual variability over northern Africa and tropical
547 SA are 0.5 GtC and 0.3 GtC respectively, larger than the 0.2 GtC and 0.1 GtC uncertainty (Figure
548 5D, E). We also find collocation of regions with large NBE and FLUXSAT-GPP interannual
549 variability (Figure B4). The availability of flux estimates over the broadly used TransCom regions
550 make it easy to compare to previous studies. For example, we estimate that the annual net carbon
551 uptake over North America is 0.7 ± 0.1 GtC/year with 0.2 GtC variability between 2010 and 2018,
552 which agrees with 0.7 ± 0.5 GtC/year estimates based on surface CO₂ observations between 1996-
553 2007 (Peylin et al., 2013).

Deleted: the range

Deleted: by

Deleted: GCP

Deleted: of 35% in 2011 to 7% in 2015

Deleted: 39%

Deleted: 23% of fossil fuel emissions

Deleted: GCP

Deleted: 25%

Deleted: 28%

Deleted: of fossil fuel emissions

Deleted: (

Deleted: ,

Deleted:)

Deleted: S4

569 **4.3 Interannual variabilities and uncertainties**

570 Here we present hemispheric and regional NBE interannual variabilities and corresponding
571 uncertainties (Figures 6 and 7, and corresponding tabular data files). In Figure 6, we further divide
572 the globe into three large latitude bands: tropics (20°S–20°N), NH extra-tropics (20°N–85°N), and
573 SH extra-tropics (60°S–20°S). The tropical NBE contributes 90% to the global NBE interannual
574 variability (IAV). The IAV of NBE over the extra-tropics is only about one-third of that over the
575 tropics. The dominant role of tropical NBE in the global IAV of NBE agrees with Figure 4 in
576 Sellers et al. (2018). The top-down global annual NBE anomaly is within the 1.0 GtC/yr
577 uncertainty of residual NBE (i.e., fossil fuel – atmospheric growth – ocean sink) calculated from
578 [GCB-2019](#) (Friedlinston et al., 2019) (Figure 6).

Deleted: GCP

579
580 Figure 7 shows the annual NBE anomalies and uncertainties over a few selected regions based on
581 RM1. Positive NBE indicates reduced net uptake relative to the 2010–2018 mean, and vice versa.
582 Also shown in Figure 7 are GPP anomalies estimated from FLUXSAT. Positive GPP indicates
583 increased productivity, and vice versa. GPP drives NBE in years where anomalies are inversely
584 correlated (e.g., positive NBE and negative GPP), and TER drives NBE in years where anomalies
585 of GPP and NBE have the same sign or are weakly correlated. Over tropical SA evergreen
586 broadleaf forest, the largest positive NBE anomalies occur during the 2015–2016 El Niño,
587 corresponding to large reductions in productivity, consistent with Liu et al. (2017). In 2017, the
588 region sees increased net uptake and increased productivity, implying a recovery from the 2015–
589 2016 El Niño event. The variability in GPP explains 80% of NBE variability over this region over
590 the nine-year period. In Australian shrubland, our inversion captures the increased net uptake in
591 2010 and 2011 due to increased precipitation (Poulter et al., 2014) and increased productivity. The

593 variability in GPP explains 70% of the interannual variability in NBE. Over tropical south America
594 savanna, the NBE interannual variability also shows strong negative correlations with GPP, with
595 GPP explaining 40% of NBE interannual variability. Over the mid-latitude regions where the IAV
596 is small, the R^2 between GPP and NBE is also small (0.0–0.5) as expected. But the increased net
597 uptake generally corresponds to increased productivity. We also do not expect perfect negative
598 correlation between NBE anomalies and GPP anomalies, as discussed in section 2.5. The
599 comparison between NBE and GPP provides insight into when and where net fluxes are likely
600 dominated by productivity.

601

602 **4.4 Seasonal cycle**

603 We provide the regional mean NBE seasonal cycle, its variability, and uncertainty based on the
604 three regional masks (Table 5). Here we briefly describe the characteristics of the NBE seasonal
605 cycle over the 11 TransCom regions, and its comparison to three independent top-down inversion
606 results based on surface CO_2 , which are CT-Europe (e.g., van der Laan-Luijkx et al., 2017) CAMS
607 (Chevallier et al., 2005), and Jena CarbonScope (Rödenbeck et al., 2003). CMS-Flux-NBE differs the
608 most from surface- CO_2 based inversions over the South American Tropical, Northern Africa,
609 tropical Asia, and NH boreal regions. The CMS-Flux NBE has a larger seasonal cycle amplitude
610 over tropical Asia and Northern Africa, where the surface CO_2 constraint is weak, while it has a
611 smaller seasonal cycle amplitude over the boreal region; this may be due to the sparse satellite
612 observations over the high latitudes and weaker seasonal amplitude of the prior CARDAMOM
613 fluxes. The comparison to FluxSat GPP can only qualitatively evaluate the NBE seasonal cycle,
614 but cannot differentiate among different estimates. In general, the months that have larger
615 productivity corresponds to months with a net uptake of carbon from the atmosphere, especially

616 over the NH (Figure 8). More research is still needed to understand the seasonal cycles of NBE,
617 including its phase (i.e., transition from source to sink) and amplitude (peak-to-trough difference),
618 and its relationships with GPP and respiration.

619

620 **5 Evaluation against independent aircraft CO₂ observations**

621 **5.1 Comparison to aircraft observations over nine sub-regions**

622 In this section, we evaluate posterior CO₂ against aircraft observations over the nine sub-regions
623 listed in Table 4 and Figure 2. We compare the posterior CO₂ to aircraft CO₂ mole fractions above
624 the planetary boundary layer and up to mid troposphere (1–5 km) at the locations and time of
625 aircraft observations, and then calculate the monthly mean error statistics between 1–5 km. The
626 aircraft observations between 1–5 km are more sensitive to regional fluxes (Liu et al., 2015; Liu
627 and Bowman, 2016). Scatter plots in the left column of Figure 9 show regional monthly mean de-
628 trended aircraft CO₂ observations (x-axis) versus the simulated detrended posterior CO₂ (y-axis).
629 We used the NOAA global CO₂ trend to detrend both the observations and model simulated mole
630 fractions (ftp://aftp.cmdl.noaa.gov/products/trends/co2/co2_trend_gl.txt). Over the NH regions (A,
631 B, C, D) and Africa (F), the R^2 is greater than or equal to 0.9, which indicates that the posterior
632 CO₂ captures the observed seasonality. The low R^2 (0.7) value in South Asia is caused by one
633 outlier. Over the Southern Ocean, Australia, and SA, the R^2 is between 0.2 and 0.4, reflecting
634 weaker CO₂ seasonality over these regions and possible bias in ocean flux estimates (see
635 discussions later).

636

637 The right panel of Figure 9 shows the monthly mean differences between posterior CO₂ and aircraft
638 observations (black), $RMSE$ (equation 2) (blue line), and $RMSE_{MC}$ (equation 3) (red line). The

639 magnitude of the mean differences between the posterior CO₂ and aircraft observations is less than
640 0.5 ppm except over the Southern Ocean, which has a -0.8 ppm bias. The mean differences between
641 posterior CO₂ and aircraft observations are primarily caused by errors in transport and biases in
642 assimilated satellite observations, while $RMSE_{MC}$ is ‘internal flux error’ projected into mole
643 fraction space. With the exception of the Southern Ocean, for all regions mean bias is significantly
644 less than $RMSE_{MC}$, which suggests that transport and data bias in satellite observations may be
645 much smaller than the internal flux errors. Note that $RMSE_{MC}$ is smaller than $RMSE$ over the first
646 ~six months of simulation, which may indicate a dominant impact of errors in transport and initial
647 CO₂ concentration on posterior CO₂ $RMSE$.

648

649 As demonstrated in section 2.5, comparing $RMSE$ and $RMSE_{MC}$ is a test of the accuracy of posterior
650 flux uncertainty estimate. Over all the regions, the differences between $RMSE$ and $RMSE_{MC}$ are
651 smaller than 0.3 ppm, which indicates a comparable magnitude between empirical posterior flux
652 uncertainty estimates from the Monte Carlo method and the actual posterior flux uncertainty over
653 the regions that these aircraft observations are sensitive to. These aircraft observations are sensitive
654 to NBE over a broad region as shown in Figure B5. Note, Figure B5 and Figures B8-B10 are
655 calculated using equation (8).

656

657 5.2 Comparison to aircraft observations from ATom and HIPPO aircraft campaigns

658 Figures 10 and 11 show comparisons to aircraft CO₂ from ATom 1–4 campaigns spanning four
659 seasons, and HIPPO 3–5 over the Pacific Ocean between 1–5 km. The vertical curtain comparisons
660 are shown in Figure B6 and B7. The mean differences between posterior CO₂ and aircraft CO₂ are
661 quite uniform (within 0.5 ppm) throughout the column except over the Atlantic Ocean during

Deleted: S5

Deleted: S5

Deleted: S8

Deleted: S10

Deleted: S6

Deleted: S7

668 ATom 1–2 and the Southern Ocean during ATom 1 (Figures S6 and S7). Also shown in Figures
669 10 and 11 are $RMSE$ of each aircraft campaign (middle column) and the ratio between $RMSE$ and
670 $RMSE_{MC}$ (right column). A ratio larger than one between $RMSE$ and $RMSE_{MC}$ indicates errors in
671 either transport or underestimation of the posterior flux uncertainty (section 2.5).

672

673 Over most of the flight tracks during ATom 1–4, the posterior CO_2 errors are between -0.5 and 0.5
674 ppm, the $RMSE$ is smaller than 0.5 ppm, and the ratio between $RMSE$ and $RMSE_{MC}$ is smaller than
675 or equal to 1. However, off the coast of Africa during ATOM -1 and -2 and over the Southern
676 Ocean during ATOM-1, the mean differences between posterior CO_2 and aircraft observations are
677 larger than 0.5 ppm. During ATOM-1 (29 July – 23 Aug 2016), the mean differences between
678 posterior CO_2 and aircraft CO_2 show large negative biases, while during ATOM-2 (26 Jan 2017–
679 21 Feb 2017), it has large positive biases off the coast of Africa. The ratio between $RMSE$ and
680 $RMSE_{MC}$ is significantly larger than one over these regions, which indicates an underestimation of
681 posterior flux uncertainty or large magnitude of transport errors during that time period.

682

683 We further run adjoint sensitivity analyses over the three regions with ratios significantly larger
684 than one to identify the posterior fluxes that could contribute to the large differences between
685 posterior CO_2 and aircraft observations during ATOM 1–2. We run the adjoint model backward
686 for three months from the observation time and calculate S_i as defined in equation (7). The adjoint
687 sensitivity analysis indicates that the large mismatch between aircraft observations and model
688 simulations during ATOM-1 and -2 off the coast of Africa could be potentially driven by errors in
689 posterior fluxes over tropical Africa (Figure B8). The large posterior CO_2 errors and large ratio
690 between $RMSE$ and $RMSE_{MC}$ over the Southern Ocean during ATOM-1 are driven by flux errors

Deleted: S8

in oceanic fluxes around 30°S and over Australia (Figure B9), which also contribute to the large errors in comparison to aircraft observations over the Southern Ocean shown in Figure 9 H.

Deleted: S9

During the HIPPO aircraft campaigns, the absolute errors in posterior CO₂ across the Pacific are less than 0.5 ppm except over the Arctic Ocean and over Alaska in summer (Figure 11), consistent with Figure 10A. The large errors over the Arctic Ocean may be related to both transport errors and the accuracy of high latitude fluxes. Byrne et al. (2020) provide a brief summary of the challenges in simulating CO₂ over high latitudes using a transport model with 4° x 5° resolution. Increasing the resolution of the transport model may reduce transport errors over high latitudes.

We run adjoint sensitivity analysis over the high-latitude regions where the differences between posterior CO₂ and aircraft observations are large (Figure 11). The adjoint sensitivity analysis (Figure B10) shows that the large errors over these regions could be driven by errors in fluxes over Alaska as well as broad NH mid-latitude regions.

Deleted: S10

5.3 Comparison to MBL reference sites

Since MBL reference sites sample air over broad regions, the comparison to detrended MBL observations indirectly evaluates the NBE over large regions. Figure 12 shows the comparison over four latitude bands. The uncertainty of posterior CO₂ concentration is from the MC method. Except over 90°S-20°S, the differences between observations and posterior CO₂ are within posterior CO₂ uncertainty estimates. The posterior CO₂ concentrations have the smallest bias and random errors over the tropical latitude band. The R² is above 0.9 over NH mid to high latitudes, consistent with Figure 9. Over 90°S-20°S, the posterior CO₂ has positive bias in 2013 and 2014

and negative bias and much weaker seasonality between Jan 2015 – Dec 2018 compared to observations, which indicates possible biases in Southern Ocean flux estimates (Figure B11). The low bias over the Southern Ocean is consistent with aircraft comparison during OCO-2 period (Figures 9-10, Figure B9). The changes of performance after 2013 over 90°S-20°S is most likely due to the prior ocean carbon fluxes. Evaluation of ocean carbon fluxes is out of scope of this study. Note, since we only assimilate land-nadir X_{CO_2} observations in this study due to known issues with the OCO-2 v9 ocean glint observations (O'Dell et al., 2018), the constraint of top-down inversion on air-sea CO_2 exchanges is weak (not shown). The ocean glint observations of OCO-2 v10 observations have been improved compared to v9 (Osterman et al., 2020). We expect to have better estimate of ocean carbon fluxes over the Southern Ocean when assimilating both land and ocean X_{CO_2} observations from GOSAT and OCO-2 in the future.

6 Discussion

Evaluation of posterior flux uncertainty estimates by comparing posterior CO_2 error statistics ($RMSE$, Equation 2) with the standard deviation of ensemble simulated CO_2 from Monte Carlo uncertainty quantification method ($RMSE_{MC}$, equation 3) has its limitations. A comparable $RMSE$ and $RMSE_{MC}$ indicates a small magnitude of transport errors and reasonable posterior uncertainty estimates. A much larger $RMSE$ than $RMSE_{MC}$ could be due to errors in either transport or underestimation of the posterior flux uncertainty or both. The presence of transport errors makes the interpretation of the $RMSE$ and $RMSE_{MC}$ complex. A better, independent quantification of transport errors is needed in the future in order to rigorously use the comparison statistics between aircraft observations and posterior CO_2 to diagnose flux errors.

Deleted: S11

Deleted: S9

742 Comparison to aircraft observations shows regionally-dependent accuracy in posterior fluxes.
743 ATom observations show seasonally-dependent biases over the Atlantic, implying possible
744 seasonally dependent errors in posterior fluxes over northern to central Africa. Therefore, we
745 recommend combining NBE with other ancillary variables, e.g., GPP, to better understand carbon
746 dynamics. Combining NBE with component carbon fluxes can shed light on the processes
747 controlling the changes of NBE (e.g., Bowman et al, 2017; Liu et al., 2017). NBE can be written
748 as:

749
$$\text{NBE} = \text{TER} + \text{fire} - \text{GPP} \quad (8)$$

750 where TER is total ecosystem respiration (TER) (Figure 1). Satellite carbon monoxide (CO)
751 observations provide constraints on fire emissions (Arellano et al, 2006, van der Werf, 2008; Jones
752 et al, 2009; Jiang et al., 2015, Bowman et al, 2017; Liu et al., 2017). In addition to the FLUXSAT-
753 GPP product used here, solar induced chlorophyll fluorescence (SIF) can be directly used as a
754 proxy for GPP (e.g., Parazoo et al, 2014). Once NBE, fire, and GPP carbon fluxes are quantified,
755 TER can be calculated as a residual (e.g., Bowman et al, 2017; Liu et al., 2017, 2018).

756
757 Because of the diffusive manner of atmospheric transport and the limited observation coverage,
758 the gridded flux values are not independent from each other. The errors and uncertainties of the
759 fluxes at each individual grid point are larger than regional aggregated fluxes. Interpreting NBE at
760 each individual grid point requires caution. But at the same time, satellite CO₂ constrained NBE
761 can potentially resolve fluxes at spatial scales smaller than the traditional TransCom regions. Here,
762 we provide regional fluxes at two predefined regions in addition to TransCom. We encourage data
763 users to use the data at appropriate regional scales.

764

765 The variability and changes are more robust than the mean NBE fluxes from top-down flux
766 inversions in general (Baker et al., 2006b). The errors in transport and potential biases in
767 observations are mostly stable in time, so biases in the mean fluxes tend to cancel out when
768 computing interannual variability and year-to-year changes (Schuh et al., 2019; Crowell et al.,
769 2019).

770

771 The global fossil fuel emissions have ~5% uncertainty (GCB-2019). However, they are regionally
772 inhomogeneous. We neglect the uncertainties in fossil fuel emissions, which will introduce
773 additional error in regions of rapid fossil fuel growth or in areas with noisier statistics (Yin et al.,
774 2019). In the future, we will account for uncertainties in fossil fuel emissions.

775

776 The posterior NBE includes all types of land fluxes except fossil fuel emissions, which is
777 equivalent to the sum of land use change fluxes, land sinks, and residual imbalance published by
778 the GCB-2019. The sum of regional NBE and fossil fuel emissions is an index of the contribution
779 of any specific region to the changes of the atmospheric CO₂ growth rate. Since the predicted
780 changes of NBE in the future have large uncertainties (Lovenduski and Bonan, 2017), quantifying
781 regional NBE is critical to monitoring regional contributions to atmospheric CO₂ growth rate, and
782 ultimately to guide mitigation to limit warming to 1.5°C above pre-industrial levels (IPCC, 2018).

783

784 7 Summary

785 Terrestrial biosphere carbon fluxes are the largest contributor to the interannual variability of the
786 atmospheric CO₂ growth rate. Therefore, monitoring its change at regional scales is essential for
787 understanding how it responds to CO₂, climate and land use. Here, we present the longest terrestrial

Deleted: P,

Deleted:

Deleted: and

Deleted: GCP

Deleted: Even over the continental US, where fossil fuel emissions are ~1.5 GtC/year, the changes of regional NBE can significantly modify contributions to the changes of atmospheric CO₂ (Liu et al., 2018).

Deleted: NBE has high variability and its

Deleted: are likely to

Deleted: IPCC, AR6

799 flux estimates and their uncertainties constrained by X_{CO_2} from 2010–2018 on self-consistent
800 global and regional scales (CMS-Flux NBE 2020). We qualitatively evaluate the NBE estimates
801 by comparing its variability with GPP variability, and provide comprehensive evaluation of
802 posterior fluxes and the uncertainties by comparing posterior CO_2 with independent CO_2
803 observations from aircraft and the NOAA MBL reference sites. This dataset can be used in
804 understanding controls on regional NBE interannual variability, evaluating biogeochemical
805 models, and supporting the monitoring of regional contributions to changes in atmospheric CO_2 .

806

807 **8 Data availability and future update**

808 The CMS-Flux NBE 2020 data are available at: <https://doi.org/10.25966/4v02-c391> (Liu et al.,
809 2020). The regional aggregated fluxes are provided as *csv* files with file size ~10MB, and the
810 gridded data is provided in NetCDF format with file size ~1.4 GB. The full ensemble of posterior
811 fluxes used to estimate posterior flux uncertainties are provided in NetCDF format with file size
812 ~30MB. Table 7 lists the sources of the data used in producing and evaluating the CMS-Flux NBE
813 2020 data product.

814

815 The quality of X_{CO_2} from satellite observations is continually improving. The OCO-2 v10 X_{CO_2}
816 has been released in June 2020 along with the full GOSAT record (June 2009–Jan 2020) processed
817 by the same retrieval algorithm as OCO-2. Continuing to improving the quality of satellite
818 observations and extending the NBE estimates beyond 2018 in the future will help us better
819 understand interactions between terrestrial biosphere carbon cycle and climate and provide support
820 in monitoring the regional contributions to the changes of atmospheric CO_2 . Thus, we plan a future

821 update of the dataset on an annual basis, with a goal to support current scientific research and
822 policy making.

823 **9 Author contributions**

824 JL designed the study and led the writing of the paper in close collaboration with KB and DS. LB
825 helped generate the plots and created all the data files. AAB provided the prior of the terrestrial
826 biosphere carbon fluxes. NP helped interpret the GPP evaluation. DM and DC generated the prior
827 ocean carbon fluxes. TO generated the ODIAC fossil fuel emissions. JJ provided the FLUXSAT
828 GPP product. BD and SW provided and contributed to the interpretation of HIPPO aircraft CO₂
829 observation comparisons. BS, KM, and CS provided ORCAS aircraft CO₂ observations and
830 contributed interpretation of aircraft CO₂ observation comparisons. LVG and JM provided INPE
831 aircraft CO₂ observations and contributed interpretation of aircraft CO₂ observation comparisons.
832 CS and KM provided ATom and the NOAA aircraft CO₂ observations and contributed
833 interpretation of aircraft CO₂ observation comparisons. We furthermore acknowledge funding
834 from the EU for the ERC project “ASICA” (grant number 649087) to Wouter Peters (Groningen
835 University) and EU and NERC (UK) funding to Emanuel Gloor (University of Leeds), which
836 contributed to the INPE Amazon greenhouse sampling program. All authors contributed to the
837 writing, and have reviewed and approved the paper.

838 **10 Competing interest**

839 The authors declare that they have no conflict of interest.

840 **Acknowledgement**

841 Resources supporting this work were provided by the NASA High-End Computing (HEC)
842 Program through the NASA Advanced Supercomputing (NAS) division at Ames Research Center.
843 We acknowledge the funding support from NASA OCO-2/3 Science Team, Carbon Monitoring

844 System (CMS), and Making Earth Science Data Records for Use in Research Environments
 845 (MEaSUREs) programs. Tomohiro Oda is supported by the NASA Carbon Cycle Science program
 846 (grant no. NNX14AM76G). We acknowledge EU and NERC (UK) funding to Emanuel Gloor,
 847 University of Leeds which substantially contributed to the INPE Amazon greenhouse sampling
 848 program. CarbonTracker Europe results provided by Wageningen University in collaboration with
 849 the ObsPack partners (<http://www.carbontracker.eu>). Part of the research was carried out at Jet
 850 Propulsion Laboratory, Caltech.

851

852 **Appendix A**

853 As shown in Kalnay (2003):

$$854 \quad RMSE^2 = \frac{1}{n} \sum_{i=1}^n (R_{i,i} + (HP^a H^T)_{i,i}) \quad (A.1)$$

855 where $R_{i,i}$ is the i^{th} aircraft observation error variance, and P^a is the posterior flux error covariance.

856 The H is linearized observation operator, which transfers posterior flux errors to aircraft
 857 observation space, and H^T is its adjoint. In the Monte Carlo method, the posterior flux error
 858 covariance P^a is approximated by:

$$859 \quad P^a = \frac{1}{n_{ens}} X^a X^{aT} \quad (A.2)$$

860 where X^a is the ensemble perturbations written as:

$$861 \quad X^a = x^a - \bar{x}^a \quad (A.3)$$

862 where x^a is the ensemble posterior fluxes from Monte Carlo, and \bar{x}^a is the mean.

863 Therefore, $HP^a H^T$ can be written as:

$$864 \quad HP^a H^T = \frac{1}{n_{ens}} [h(x^a) - h(\bar{x}^a)][h(x^a) - h(\bar{x}^a)]^T \quad (A.4)$$

865 The sum of diagonal elements in the right-hand side of A.4 is the same as the definition of $RMSE_{MC}$
 866 in the main text.

867 Therefore, when the posterior flux uncertainty estimated by Monte Carlo method represents the
868 actual uncertainty in posterior fluxes, equation (A.1) can be written as:

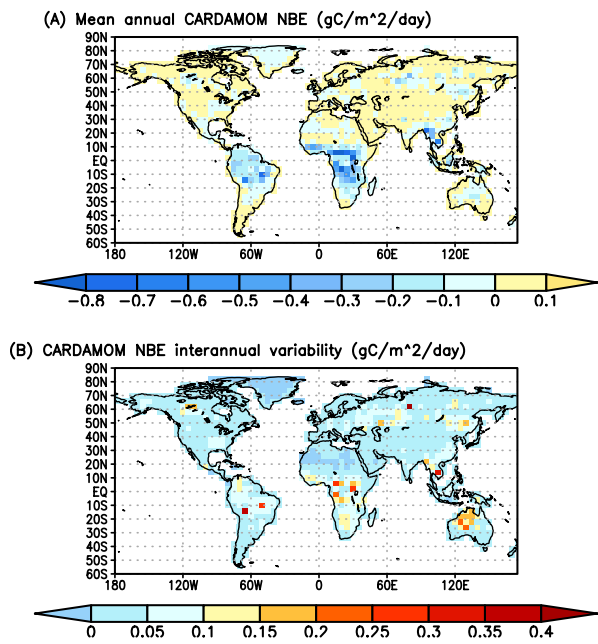
869
$$RMSE^2 = \frac{1}{n} \sum_{i=1}^n R_{i,i} + RMSE_{MC}^2 \quad (A.5).$$

870 It is the same as equation (4) in the main text.

871 **Appendix B**

872 In this Appendix, we include figures to support the main text.

Formatted: Font: Not Bold
Formatted: Font: Not Bold



873
874 **Figure B1 Annual mean net biosphere exchanges from CARDAMOM (A) and its interannual**
875 **variability between 2010 and 2017 (B).**

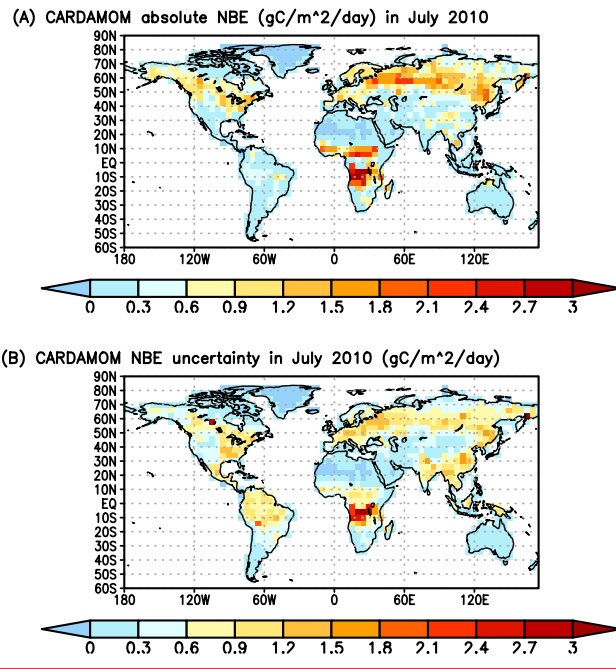


Figure B2 An example of absolute mean NBE (A) and its uncertainty (B) simulated by CARDAMOM. This is for July 2010.

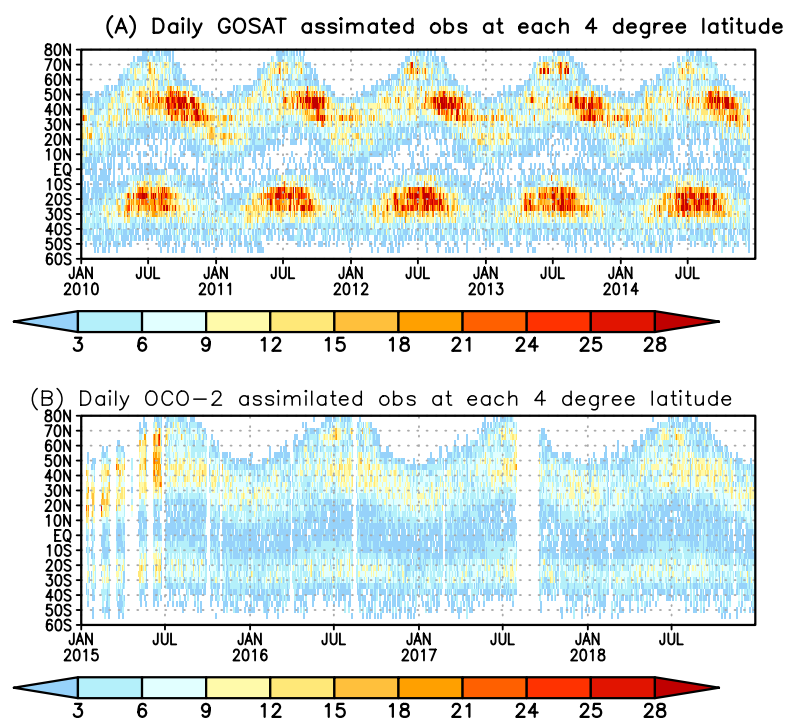


Figure B3 Daily number of ACOS-GOSAT b7.3 (A) and OCO-2 super observations (B) assimilated in the top-down inversions.

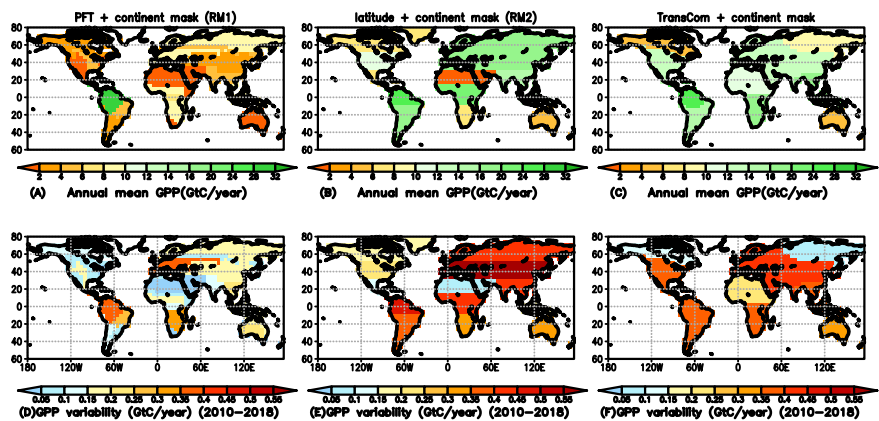


Figure B4 Regional mean FIUXSAT GPP and its variability between 2010–2018. (A, B, and C) Regional mean GPP aggregated with the three regional masks; (D, E, and F) GPP variability between 2010–2018. Unit: GtC/year.

The sensitivity of RMSE to
posterior fluxes over (2015–2018) (%)

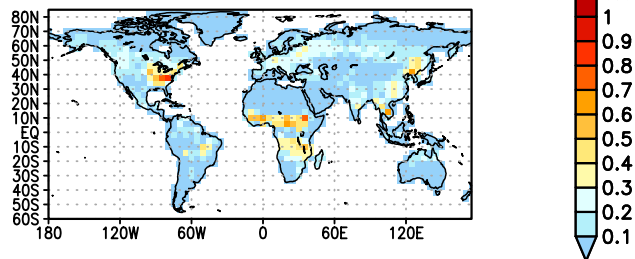
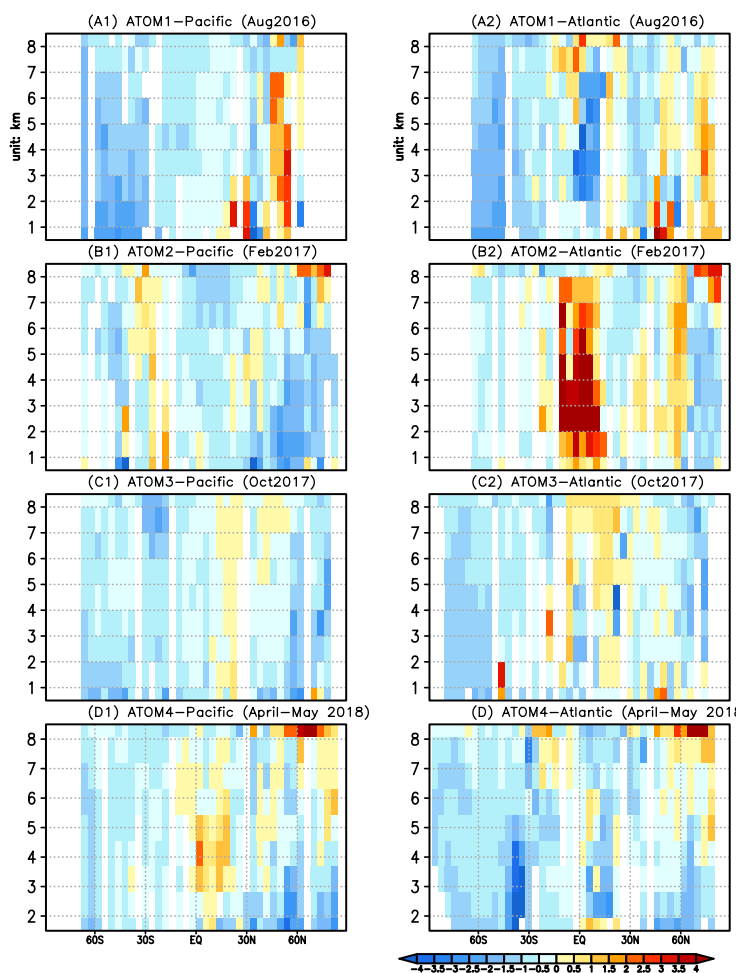


Figure B5 The relative sensitivity of root mean square errors (RMSE) of posterior CO₂ (Figure 9 in the main text) relative to NBE at every grid point. The adjoint model is carried out over Sep 2014–Dec 2018.

p04



p05

p06

p07

p08

p09

p10

Figure B6 Differences between posterior CO₂ and ATOM 1-4 aircraft CO₂ observations over the Pacific (A1-D1) and Atlantic Ocean (A2-D2) as a function of latitude and altitude (unit: km). Unit: ppm.

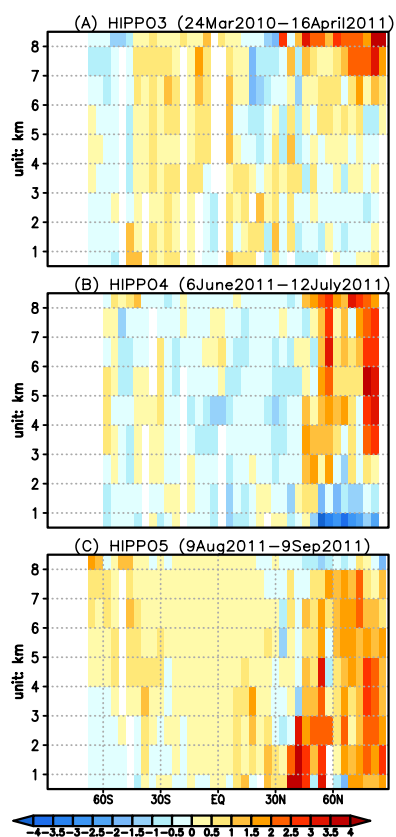
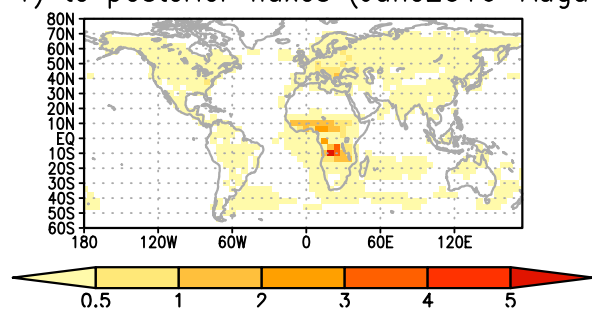


Figure B7 Differences between posterior CO₂ and HIPPO 3-5 aircraft CO₂ observations over the Pacific (A-C) as a function of latitude and altitude. Unit: ppm.

A.Relative sensitivity of RMSE between 40W–0, 20S–20N (ATOM–1) to posterior fluxes (June2016–August2016)



B.Relative sensitivity of RMSE between 40W–0, 20S–20N (ATOM–2) to posterior fluxes (Dec2016–Feb2017)

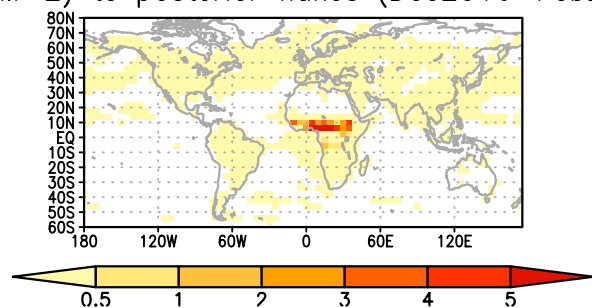


Figure B8 The relative sensitivity of RMSE of posterior CO₂ to NBE over land and air-sea net carbon exchange over ocean at every grid point. The RMSE is calculated against aircraft CO₂ observations from ATom-1 (A) and ATom-2 (B) between 40°W–0°, 20°S–20°N. The adjoint model is carried out over June – August 2016 (A) and Dec 2016 – Feb 2017 (B). Unit: %.

Relative sensitivity of RMSE between 175W–20W, 80S–30S
(ATOM-1) to posterior fluxes (June–August)

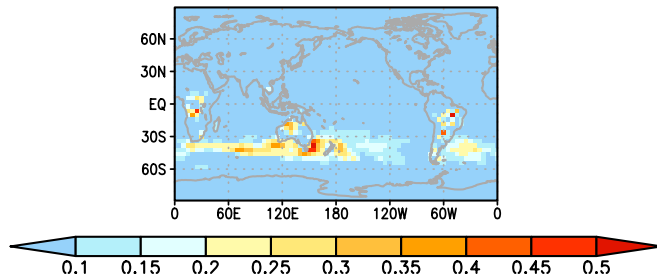


Figure B9 The relative sensitivity of RMSE of posterior to NBE over land and air-sea net carbon exchange over ocean at every grid point. The RMSE is calculated against aircraft CO₂ observations from ATom-1 between 175°W–20°W, 80°S–30°S. The adjoint model is carried out over June – August 2016. Unit: %.

Relative sensitivity of RMSE between 180W–130W, 50N–90N
(HIPPO-4) to posterior fluxes (Apr–July)

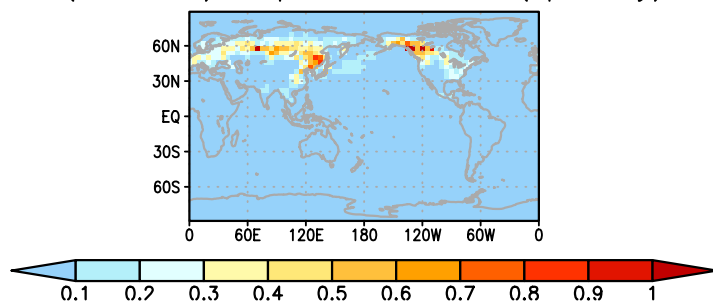


Figure B10 The relative sensitivity of RMSE of posterior to NBE over land and air-sea net carbon exchange over ocean at every grid point. The RMSE is calculated against aircraft CO₂ observations from HIPPO-4 between 180°W-130°W, 50°N-90°N. The adjoint model is carried out over April – July 2011. Unit: %.

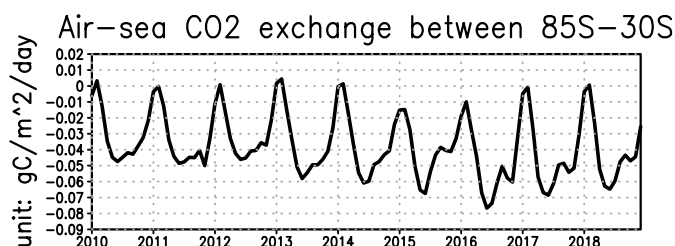


Figure B11 Monthly posterior air-sea CO₂ exchanges between 85°S-30°S. (unit: gC/m²/day)

References

- Arellano Jr, A.F., Kasibhatla, P.S., Giglio, L., Van der Werf, G.R., Randerson, J.T., and Collatz, G.J.: Time-dependent inversion estimates of global biomass-burning CO emissions using Measurement of Pollution in the Troposphere (MOPITT) measurements, *J. Geophys. Res. Atmos.*, 111, D09303, <https://doi.org/10.1029/2005JD006613>, 2006.
- Baker, D.F., Doney, S.C., and Schimel, D.S.: Variational data assimilation for atmospheric CO₂, *Tellus B: Chem. Phys. Meteorol.*, 58, 359-365, <https://doi.org/10.1111/j.1600-0889.2006.00218.x>, 2006a.
- Baker, D.F., Law, R.M., Gurney, K.R., Rayner, P., Peylin, P., Denning, A.S., Bousquet, P., Bruhwiler, L., Chen, Y.H., Ciais, P., and Fung, I.Y.: TransCom 3 inversion intercomparison: Impact of transport model errors on the interannual variability of regional CO₂ fluxes, 1988–2003, *Global Biogeochem. Cy.*, 20, GB1002, <https://doi.org/10.1029/2004GB002439>, 2006b.
- Bastos, A., Friedlingstein, P., Sitch, S., Chen, C., Mialon, A., Wigneron, J.-P., Arora, V. K., Briggs, P. R., Canadell, J. G., and Ciais, P.: Impact of the 2015/2016 El Niño on the terrestrial carbon cycle constrained by bottom-up and top-down approaches. *Philos. Trans. R Soc. Lond. B. Biol. Sci.*, 373, 1760, <https://doi.org/10.1098/rstb.2017.0304>, 2018.
- Bloom, A.A., Exbrayat, J.F., van der Velde, I.R., Feng, L., and Williams, M.: The decadal state of the terrestrial carbon cycle: Global retrievals of terrestrial carbon allocation, pools, and residence times. *Proc. Natl Acad. Sci.*, 113, 1285-1290, 2016.
- Bloom, A. A., Bowman, K. W., Liu, J., Konings, A. G., Worden, J. R., Parazoo, N. C., Meyer, V., Reager, J. T., Worden, H. M., Jiang, Z., Quetin, G. R., Smallman, T. L., Exbrayat, J.-F., Yin, Y., Saatchi, S. S., Williams, M., and Schimel, D. S.: Lagged effects dominate the inter-annual variability of the 2010–2015 tropical carbon balance, *Biogeosciences Discuss.*, <https://doi.org/10.5194/bg-2019-459>, in review, 2020.

1007 Bowman, K.W., Liu, J., Bloom, A.A., Parazoo, N.C., Lee, M., Jiang, Z., Menemenlis, D., Gierach,
 1008 M.M., Collatz, G.J., Gurney, K.R., and Wunch, D.: Global and Brazilian carbon response to El
 1009 Niño Modoki 2011–2010, *Earth Space Sci.*, 4, 637-660, <https://doi.org/10.1002/2016EA000204>,
 1010 2017.
 1011
 1012 Brix, H., Menemenlis, D., Hill, C., Dutkiewicz, S., Jahn, O., Wang, D., Bowman, K., and Zhang,
 1013 H.: Using Green's Functions to initialize and adjust a global, eddying ocean biogeochemistry
 1014 general circulation model, *Ocean Model.*, 95, 1-14, <https://doi.org/10.1016/j.ocemod.2015.07.008>,
 1015 2015.
 1016
 1017 Byrd, R.H., Nocedal, J., and Schnabel, R.B.: Representations of quasi-Newton matrices and their
 1018 use in limited memory methods, *Math. Program.*, 63, 129-156,
 1019 <https://doi.org/10.1007/BF01582063>, 1994.
 1020
 1021 Byrne, B., Liu, J., et al.: Improved constraints on northern extratropical CO₂ fluxes obtained by
 1022 combining surface-based and space-based atmospheric CO₂ measurements, *JGR-Atmosphere*,
 1023 (*minor revision*), 2020
 1024
 1025 Carroll, D., Menemenlis, D., Adkins, J. F., Bowman, K. W., Brix, H., Dutkiewicz, S., et al.:
 1026 The ECCO-Darwin Data-assimilative Global Ocean Biogeochemistry Model: Estimates of Seasonal to
 1027 Multi-decadal Surface Ocean pCO₂ and Air-sea CO₂ Flux. *Journal of Advances in Modeling Earth*
 1028 *Systems*, 12, e2019MS001888. <https://doi.org/10.1029/2019MS001888>, 2020
 1029
 1030 Carbontracker Team; (2019) : Compilation of near real time atmospheric carbon dioxide data;
 1031 obspack_co2_1_NRT_v5.0_2019-08-13; NOAA Earth System Research Laboratory, Global
 1032 Monitoring Division. <http://doi.org/10.25925/20190813>
 1033
 1034 Chevallier, F., Fisher, M., Peylin, P., Serrar, S., Bousquet, P., Bréon, F.M., Chédin, A., and Ciais,
 1035 P.: Inferring CO₂ sources and sinks from satellite observations: Method and application to TOVS
 1036 data, *J. Geophys. Res.-Atmos.*, 110, D24309, <https://doi.org/10.1029/2005JD006390>, 2005.
 1037
 1038 Chevallier, F., Ciais, P., Conway, T.J., Aalto, T., Anderson, B.E., Bousquet, P., Brunke, E.G.,
 1039 Ciattaglia, L., Esaki, Y., Fröhlich, M., and Gomez, A.: CO₂ surface fluxes at grid point scale
 1040 estimated from a global 21 year reanalysis of atmospheric measurements, *J. Geophys. Res.*, 115,
 1041 D21307, <https://doi.org/10.1029/2010JD013887>, 2010.
 1042
 1043 Chevallier, F., Remaud, M., O'Dell, C. W., Baker, D., Peylin, P., and Cozic, A.: Objective
 1044 evaluation of surface- and satellite-driven carbon dioxide atmospheric inversions, *Atmos. Chem.*
 1045 *Phys.*, 19, 14233–14251, <https://doi.org/10.5194/acp-19-14233-2019>, 2019.
 1046
 1047 Ciais, P., Tan, J., Wang, X., Roedenbeck, C., Chevallier, F., Piao, S.L., Moriarty, R., Broquet, G.,
 1048 Le Quéré, C., Canadell, J.G., and Peng, S.: Five decades of northern land carbon uptake revealed
 1049 by the interhemispheric CO₂ gradient, *Nature*, 568, 221-225, <https://doi.org/10.1038/s41586-019-1078-6>, 2019.
 1050
 1051
 1052 Conway, T. J., Tans, P. P., Waterman, L. S., Thoning, K. W., Kitzis, D. R., Masarie, K. A.,
 1053 and Zhang, N. (1994), Evidence for interannual variability of the carbon cycle from the National

1054 Oceanic and Atmospheric Administration/Climate Monitoring and Diagnostics Laboratory Global
 1055 Air Sampling Network, *J. Geophys. Res.*, 99(D11), 22831–22855, doi:[10.1029/94JD01951](https://doi.org/10.1029/94JD01951).
 1056
 1057
 1058 Crisp, D., Fisher, B. M., O'Dell, C., Frankenberg, C., Basilio, R., Bösch, H., Brown, L. R., Castano,
 1059 R., Connor, B., Deutscher, N. M., Eldering, A., Griffith, D., Gunson, M., Kuze, A., Mandrake, L.,
 1060 McDuffie, J., Messerschmidt, J., Miller, C. E., Morino, I., Natraj, V., Notholt, J., O'Brien, D. M.,
 1061 Oyafuso, F., Polonsky, I., Robinson, J., Salawitch, R., Sherlock, V., Smyth, M., Suto, H., Taylor,
 1062 T. E., Thompson, D. R., Wennberg, P. O., Wunch, D., and Yung, Y. L.: The ACOS CO₂ retrieval
 1063 algorithm – Part II: Global XCO₂ data characterization, *Atmos. Meas. Tech.*, 5, 687–707,
 1064 <https://doi.org/10.5194/amt-5-687-2012>, 2012.
 1065
 1066 Crisp, D., Pollock, H. R., Rosenberg, R., Chapsky, L., Lee, R. A. M., Oyafuso, F. A., Frankenberg,
 1067 C., O'Dell, C. W., Bruegge, C. J., Doran, G. B., Eldering, A., Fisher, B. M., Fu, D., Gunson, M.
 1068 R., Mandrake, L., Osterman, G. B., Schwandner, F. M., Sun, K., Taylor, T. E., Wennberg, P. O.,
 1069 and Wunch, D.: The on-orbit performance of the Orbiting Carbon Observatory-2 (OCO-2)
 1070 instrument and its radiometrically calibrated products, *Atmos. Meas. Tech.*, 10, 59–81,
 1071 <https://doi.org/10.5194/amt-10-59-2017>, 2017.
 1072
 1073 Crowell, S., Baker, D., Schuh, A., Basu, S., Jacobson, A. R., Chevallier, F., Liu, J., Deng, F., Feng,
 1074 L., McKain, K., Chatterjee, A., Miller, J. B., Stephens, B. B., Eldering, A., Crisp, D., Schimel, D.,
 1075 Nassar, R., O'Dell, C. W., Oda, T., Sweeney, C., Palmer, P. I., and Jones, D. B. A.: The 2015–
 1076 2016 carbon cycle as seen from OCO-2 and the global in situ network, *Atmos. Chem. Phys.*, 19,
 1077 9797–9831, <https://doi.org/10.5194/acp-19-9797-2019>, 2019.
 1078
 1079 [Davis, K.J., M.D. Obland, B. Lin, T. Lauvaux, C. O'Dell, B. Meadows, E.V. Browell, J.P. DiGangi,](https://doi.org/10.3334/ORNDAAC/1593)
 1080 [C. Sweeney, M.J. McGill, J.D. Barrick, A.R. Nehrir, M.M. Yang, J.R. Bennett, B.C. Baier, A.](https://doi.org/10.3334/ORNDAAC/1593)
 1081 [Roiger, S. Pal, T. Gerken, A. Fried, S. Feng, R. Shrestha, M.A. Shook, G. Chen, L.J. Campbell,](https://doi.org/10.3334/ORNDAAC/1593)
 1082 [Z.R. Barkley, and R.M. Pauly. 2018. ACT-America: L3 Merged In Situ Atmospheric Trace Gases](https://doi.org/10.3334/ORNDAAC/1593)
 1083 [and Flask Data, Eastern USA. ORNL DAAC, Oak Ridge, Tennessee, USA.](https://doi.org/10.3334/ORNDAAC/1593)
 1084 <https://doi.org/10.3334/ORNDAAC/1593>
 1085
 1086 Falk, M., Wharton, S., Schroeder, M., Ustin, S., and U, K.T.P.: Flux partitioning in an old-growth
 1087 forest: seasonal and interannual dynamics. *Tree Physiol.*, 28, 509–520,
 1088 <https://doi.org/10.1093/treephys/28.4.509>, 2008.
 1089
 1090 Fisher, M. and Courtier, P. (1995) Estimating the covariance matrices of analysis and forecast
 1091 error in variational data assimilation. Technical Memorandum 220. Reading, UK: ECMWF.
 1092
 1093
 1094 Friedlingstein, P., Meinshausen, M., Arora, V.K., Jones, C.D., Anav, A., Liddicoat, S.K., and
 1095 Knutti, R.: Uncertainties in CMIP5 climate projections due to carbon cycle feedbacks, *J. Clim.*, 27,
 1096 511–526, <https://doi.org/10.1175/JCLI-D-12-00579.1>, 2014.
 1097

Formatted: Justified

Field Code Changed

1098 Friedlingstein, P., Jones, M., O'Sullivan, M., Andrew, R., Hauck, J., Peters, G., Peters, W.,
 1099 Pongratz, J., Sitch, S., Le Quéré, C., and DBakker, O.: Global carbon budget 2019, *Earth Syst. Sci.*
 1100 *Data*, 11, 1783-1838, <https://doi.org/10.3929/ethz-b-000385668>, 2019.

1101
 1102 Gatti, L.V., Gloor, M., Miller, J.B., Doughty, C.E., Malhi, Y., Domingues, L.G., Basso, L.S.,
 1103 Martinewski, A., Correia, C.S.C., Borges, V.F., and Freitas, S., 2014, Drought sensitivity of
 1104 Amazonian carbon balance revealed by atmospheric measurements, *Nature*, 506, 76-80,
 1105 <https://doi.org/10.1038/nature12957>, 2014.

1106
 1107 Gaubert, B., Stephens, B. B., Basu, S., Chevallier, F., Deng, F., Kort, E. A., Patra, P. K., Peters,
 1108 W., Rödenbeck, C., Saeki, T., Schimel, D., Van der Laan-Luijkx, I., Wofsy, S., and Yin, Y.: Global
 1109 atmospheric CO₂ inverse models converging on neutral tropical land exchange, but disagreeing on
 1110 fossil fuel and atmospheric growth rate, *Biogeosciences*, 16, 117–134, [https://doi.org/10.5194/bg-](https://doi.org/10.5194/bg-16-117-2019)
 1111 16-117-2019, 2019.

1112
 1113
 1114 Gurney, K.R., Law, R.M., Denning, A.S., Rayner, P.J., Pak, B.C., Baker, D., Bousquet, P.,
 1115 Bruhwiler, L., Chen, Y.H., Ciais, P., and Fung, I.Y.: Transcom 3 inversion intercomparison: Model
 1116 mean results for the estimation of seasonal carbon sources and sinks, *Global Biogeochem.*
 1117 *Cycles*, 18, GB1010, <https://doi.org/10.1029/2003GB002111>, 2004.

1118
 1119 Henze, D. K., Hakami, A., and Seinfeld, J. H.: Development of the adjoint of GEOS-Chem, *Atmos.*
 1120 *Chem. Phys.*, 7, 2413–2433, <https://doi.org/10.5194/acp-7-2413-2007>, 2007.

1121
 1122 IPCC (2018). *Global warming of 1.5°C. An IPCC Special Report on the impacts of global*
 1123 *warming of 1.5°C above pre-industrial levels and related global greenhouse gas emission*
 1124 *pathways, in the context of strengthening the global response to the threat of climate change,*
 1125 *sustainable development, and efforts to eradicate poverty* [V. Masson-Delmotte, P. Zhai, H. O.
 1126 Pörtner, D. Roberts, J. Skea, P. R. Shukla, A. Pirani, W. Moufouma-Okia, C. Péan, R. Pidcock,
 1127 S. Connors, J. B. R. Matthews, Y. Chen, X. Zhou, M. I. Gomis, E. Lonnoy, T. Maycock, M.
 1128 Tignor, T. Waterfield (eds.)]. In Press.

1129
 1130 Jiang, Z., Worden, J. R., Worden, H., Deeter, M., Jones, D. B. A., Arellano, A. F., and Henze, D.
 1131 K.: A 15-year record of CO emissions constrained by MOPITT CO observations, *Atmos. Chem.*
 1132 *Phys.*, 17, 4565–4583, <https://doi.org/10.5194/acp-17-4565-2017>, 2017.

1133
 1134 Joiner, J., Guanter, L., Lindstrot, R., Voigt, M., Vasilkov, A. P., Middleton, E. M., Huemmrich, K.
 1135 F., Yoshida, Y., and Frankenberg, C.: Global monitoring of terrestrial chlorophyll fluorescence
 1136 from moderate-spectral-resolution near-infrared satellite measurements: methodology,
 1137 simulations, and application to GOME-2, *Atmos. Meas. Tech.*, 6, 2803–2823,
 1138 <https://doi.org/10.5194/amt-6-2803-2013>, 2013.

1139
 1140 Joiner, J., Yoshida, Y., Zhang, Y., Duveiller, G., Jung, M., Lyapustin, A., Wang, Y., & Tucker,
 1141 C.: Estimation of terrestrial global gross primary production (GPP) with satellite data-driven
 1142 models and eddy covariance flux data. *Remote*
 1143 *Sensing*, 10(9), 1346. <https://doi.org/10.3390/rs10091346>. 2018.

Formatted: Font: (Default) Times New Roman, 12 pt

1144 Jones, D. B. A., Bowman, K. W., Logan, J. A., Heald, C. L., Liu, J., Luo, M., Worden, J., and
 1145 Drummond, J.: The zonal structure of tropical O₃ and CO as observed by the Tropospheric
 1146 Emission Spectrometer in November 2004 – Part 1: Inverse modeling of CO emissions, *Atmos.*
 1147 *Chem. Phys.*, 9, 3547–3562, <https://doi.org/10.5194/acp-9-3547-2009>, 2009.
 1148
 1149 Jung, Martin, et al.: "Compensatory water effects link yearly global land CO₂ sink changes to
 1150 temperature." *Nature* 541.7638 (2017): 516-520.
 1151
 1152 Kiel, M., O'Dell, C. W., Fisher, B., Eldering, A., Nassar, R., MacDonald, C. G., and Wennberg, P.
 1153 O.: How bias correction goes wrong: measurement of X_{CO₂} affected by erroneous surface pressure
 1154 estimates, *Atmos. Meas. Tech.*, 12, 2241–2259, <https://doi.org/10.5194/amt-12-2241-2019>, 2019.
 1155
 1156 Konings, A. G., Bloom, A. A., Liu, J., Parazoo, N. C., Schimel, D. S., and Bowman, K. W.: Global
 1157 satellite-driven estimates of heterotrophic respiration, *Biogeosciences*, 16, 2269–2284,
 1158 <https://doi.org/10.5194/bg-16-2269-2019>, 2019.
 1159
 1160 Kulawik, S. S., Crowell, S., Baker, D., Liu, J., McKain, K., Sweeney, C., Biraud, S. C., Wofsy, S.,
 1161 O'Dell, C. W., Wennberg, P. O., Wunch, D., Roehl, C. M., Deutscher, N. M., Kiel, M., Griffith,
 1162 D. W. T., Velazco, V. A., Notholt, J., Warneke, T., Petri, C., De Mazière, M., Sha, M. K.,
 1163 Sussmann, R., Rettinger, M., Pollard, D. F., Morino, I., Uchino, O., Hase, F., Feist, D. G., Roche,
 1164 S., Strong, K., Kivi, R., Iraci, L., Shiomi, K., Dubey, M. K., Sepulveda, E., Rodriguez, O. E. G.,
 1165 Té, Y., Jeseck, P., Heikkinen, P., Dlugokencky, E. J., Gunson, M. R., Eldering, A., Crisp, D.,
 1166 Fisher, B., and Osterman, G. B.: Characterization of OCO-2 and ACOS-GOSAT biases and errors
 1167 for CO₂ flux estimates, *Atmos. Meas. Tech. Discuss.*, <https://doi.org/10.5194/amt-2019-257>, in
 1168 review, 2019.
 1169
 1170 Kuze, A., Suto, H., Shiomi, K., Kawakami, S., Tanaka, M., Ueda, Y., Deguchi, A., Yoshida, J.,
 1171 Yamamoto, Y., Kataoka, F., Taylor, T. E., and Buijs, H. L.: Update on GOSAT TANSO-FTS
 1172 performance, operations, and data products after more than 6 years in space, *Atmos. Meas. Tech.*,
 1173 9, 2445–2461, <https://doi.org/10.5194/amt-9-2445-2016>, 2016.
 1174
 1175 Le Quéré, C., Andrew, R. M., Friedlingstein, P., Sitch, S., Pongratz, J., Manning, A. C.,
 1176 Korsbakken, J. I., Peters, G. P., Canadell, J. G., Jackson, R. B., Boden, T. A., Tans, P. P., Andrews,
 1177 O. D., Arora, V. K., Bakker, D. C. E., Barbero, L., Becker, M., Betts, R. A., Bopp, L., Chevallier,
 1178 F., Chini, L. P., Ciais, P., Cosca, C. E., Cross, J., Currie, K., Gasser, T., Harris, I., Hauck, J., Haverd,
 1179 V., Houghton, R. A., Hunt, C. W., Hurtt, G., Ilyina, T., Jain, A. K., Kato, E., Kautz, M., Keeling,
 1180 R. F., Klein Goldewijk, K., Körtzinger, A., Landschützer, P., Lefèvre, N., Lenton, A., Lienert, S.,
 1181 Lima, I., Lombardozzi, D., Metzl, N., Millero, F., Monteiro, P. M. S., Munro, D. R., Nabel, J. E.
 1182 M. S., Nakaoka, S., Nojiri, Y., Padin, X. A., Pregon, A., Pfeil, B., Pierrot, D., Poulter, B., Rehder,
 1183 G., Reimer, J., Rödenbeck, C., Schwinger, J., Séférian, R., Skjelvan, I., Stocker, B. D., Tian, H.,
 1184 Tilbrook, B., Tubiello, F. N., van der Laan-Luijkx, I. T., van der Werf, G. R., van Heuven, S.,
 1185 Viovy, N., Vuichard, N., Walker, A. P., Watson, A. J., Wiltshire, A. J., Zaehle, S., and Zhu, D.:
 1186 Global Carbon Budget 2017, *Earth Syst. Sci. Data*, 10, 405–448, <https://doi.org/10.5194/essd-10-405-2018>, 2018.
 1187
 1188
 1189

1190 Liu, J., Baskarran, L., Bowman, K., Schimel, D., Bloom, A. A., Parazoo, N., Oda, T., Carrol, D.,
 1191 Menemenlis, D., Joiner, J., Commane, R., Daube, B., Gatti, L. V., McKain, K., Miller, J.,
 1192 Stephens, B. B., Sweeney, C., & Wofsy, S. (2020). *CMS-Flux NBE 2020* [Data set]. NASA.
 1193 <https://doi.org/10.25966/4V02-C391>
 1194
 1195 Liu, J. and Bowman, K.: A method for independent validation of surface fluxes from atmospheric
 1196 inversion: Application to CO₂, *Geophys. Res. Lett.*, 43, 3502-3508,
 1197 <https://doi.org/10.1002/2016GL067828>, 2016.
 1198
 1199 Liu, J., Bowman, K. W., and Henze, D. K.: Source-receptor relationships of column-average
 1200 CO₂ and implications for the impact of observations on flux inversions. *J. Geophys. Res.*
 1201 *Atmos.*, 120, 5214– 5236. doi: [10.1002/2014JD022914](https://doi.org/10.1002/2014JD022914), 2015
 1202
 1203 Liu, J., Bowman, K.W., Lee, M., Henze, D.K., Bousserez, N., Brix, H., James Collatz, G.,
 1204 Menemenlis, D., Ott, L., Pawson, S., and Jones, D.: Carbon monitoring system flux estimation and
 1205 attribution: impact of ACOS-GOSAT XCO₂ sampling on the inference of terrestrial biospheric
 1206 sources and sinks. *Tellus B Chem. Phys. Meteorol. B.*, 66, 22486,
 1207 <http://dx.doi.org/10.3402/tellusb.v66.22486>, 2014.
 1208
 1209 Liu, J., Bowman, K.W., Schimel, D.S., Parazoo, N.C., Jiang, Z., Lee, M., Bloom, A.A., Wunch,
 1210 D., Frankenberg, C., Sun, Y., and O'Dell, C.W.: Contrasting carbon cycle responses of the tropical
 1211 continents to the 2015–2016 El Niño. *Science*, 358, eaam5690,
 1212 <https://doi.org/10.1126/science.aam5690>, 2017.
 1213
 1214 Liu, J., Bowman, K., Parazoo, N.C., Bloom, A.A., Wunch, D., Jiang, Z., Gurney, K.R., and
 1215 Schimel, D.: Detecting drought impact on terrestrial biosphere carbon fluxes over contiguous US
 1216 with satellite observations. *Environ. Res. Lett.*, 13, 095003, [https://doi.org/10.1088/1748-](https://doi.org/10.1088/1748-9326/aad5ef)
 1217 [9326/aad5ef](https://doi.org/10.1088/1748-9326/aad5ef), 2018.
 1218
 1219 Liu, Z.-Q. and Rabier, F. (2003), The potential of high-density observations for numerical
 1220 weather prediction: A study with simulated observations. *Q.J.R. Meteorol. Soc.*, 129: 3013-3035.
 1221 doi:[10.1256/qj.02.170](https://doi.org/10.1256/qj.02.170)
 1222
 1223 Lorenc, A. C., 1981: A Global Three-Dimensional Multivariate Statistical Interpolation
 1224 Scheme. *Mon. Wea. Rev.*, **109**, 701–721
 1225
 1226 Lovenduski, N.S. and Bonan, G.B.: Reducing uncertainty in projections of terrestrial carbon
 1227 uptake, *Environ. Res. Lett.*, 12, 044020, <https://doi.org/10.1088/1748-9326/aa66b8>, 2017.
 1228
 1229 Meirink, J.F., Bergamaschi, P. and Krol, M.C. (2008) Four-dimensional variational data
 1230 assimilation for inverse modelling of atmospheric methane emissions: method and comparison
 1231 with synthesis inversion, *Atmos. Chem. Phys.*, **8**, 6341– 6353, [https://doi.org/10.5194/acp-8-](https://doi.org/10.5194/acp-8-6341-2008)
 1232 [6341-2008](https://doi.org/10.5194/acp-8-6341-2008).
 1233
 1234
 1235

1236 Nassar, R., Jones, D.B., Suntharalingam, P., Chen, J.M., Andres, R.J., Wecht, K.J., Yantosca, R.M.,
 1237 Kulawik, S.S., Bowman, K.W., Worden, J.R., and Machida, T.: Modeling global atmospheric CO₂
 1238 with improved emission inventories and CO₂ production from the oxidation of other carbon
 1239 species. *Geosci. Model Dev.*, 3, 689–716, <https://doi.org/10.5194/gmd-3-689-2010>, 2010.
 1240
 1241 Niwa, Y, Fujii, Y. A conjugate BFGS method for accurate estimation of a posterior error
 1242 covariance matrix in a linear inverse problem. *Q J R Meteorol*
 1243 *Soc.* 2020; 1– 26. <https://doi.org/10.1002/qj.3838>
 1244
 1245 Oda, T., Maksyutov, S., and Andres, R. J.: The Open-source Data Inventory for Anthropogenic
 1246 CO₂, version 2016 (ODIAC2016): a global monthly fossil fuel CO₂ gridded emissions data product
 1247 for tracer transport simulations and surface flux inversions, *Earth Syst. Sci. Data*, 10, 87–107,
 1248 <https://doi.org/10.5194/essd-10-87-2018>, 2018.
 1249
 1250 O'Dell, C. W., Connor, B., Bösch, H., O'Brien, D., Frankenberg, C., Castano, R., Christi, M.,
 1251 Eldering, D., Fisher, B., Gunson, M., McDuffie, J., Miller, C. E., Natraj, V., Oyafuso, F., Polonsky,
 1252 I., Smyth, M., Taylor, T., Toon, G. C., Wennberg, P. O., and Wunch, D.: The ACOS CO₂ retrieval
 1253 algorithm – Part 1: Description and validation against synthetic observations, *Atmos. Meas. Tech.*,
 1254 5, 99–121, <https://doi.org/10.5194/amt-5-99-2012>, 2012.
 1255
 1256 O'Dell, C., Eldering, A., Wennberg, P.O., Crisp, D., Gunson, M., Fisher, B., Frankenberg, C., Kiel,
 1257 M., Lindqvist, H., Mandrake, L., and Merrelli, A.: Improved retrievals of carbon dioxide from
 1258 Orbiting Carbon Observatory-2 with the version 8 ACOS algorithm, *Atmos. Meas. Tech.*, 11,
 1259 6539–6576, <https://doi.org/10.5194/amt-11-6539-2018>, 2018.
 1260
 1261 Olsen, S.C. and Randerson, J.T.: Differences between surface and column atmospheric CO₂ and
 1262 implications for carbon cycle research, *J. Geophys. Res: Atmos.*, 109, D02301,
 1263 <https://doi.org/10.1029/2003JD003968>, 2004.
 1264
 1265 Osterman, G., O'Dell, C., Eldering, A.: Data Product User's Guide, Operational Level 2 Data
 1266 Versions 10 and Lite File Version 10 and VEarly.
 1267 https://docsserver.gesdisc.eosdis.nasa.gov/public/project/OCO/OCO2_OCO3_B10_DUG.pdf,
 1268 2020.
 1269
 1270 Parazoo, N.C., Bowman, K., Fisher, J.B., Frankenberg, C., Jones, D.B.A., Cescatti, A., Pérez-
 1271 Priego, Ó., Wohlfahrt, G. and Montagnani, L.: Terrestrial gross primary production inferred from
 1272 satellite fluorescence and vegetation models. *Glob Change Biol*, 20: 3103–3121.
 1273 doi:[10.1111/gcb.12652](https://doi.org/10.1111/gcb.12652). 2014.
 1274
 1275 Peylin, P., Law, R. M., Gurney, K. R., Chevallier, F., Jacobson, A. R., Maki, T., Niwa, Y., Patra,
 1276 P. K., Peters, W., Rayner, P. J., Rödenbeck, C., van der Laan-Luijkx, I. T., and Zhang, X.: Global
 1277 atmospheric carbon budget: results from an ensemble of atmospheric CO₂ inversions,
 1278 *Biogeosciences*, 10, 6699–6720, <https://doi.org/10.5194/bg-10-6699-2013>, 2013.
 1279
 1280

1281 Peters, W., et al. (2007), An atmospheric perspective on North American carbon dioxide exchange:
 1282 CarbonTracker, *Proc. Natl. Acad. Sci. U. S. A.*, **104**(48), 18,925– 18,930,
 1283 doi:[10.1073/pnas.0708986104](https://doi.org/10.1073/pnas.0708986104).
 1284
 1285 Peters, W., Krol, M. C., Van Der Werf, G.R., et al, 2010, Seven years of recent European net
 1286 terrestrial carbon dioxide exchange constrained by atmospheric observations. *Global Change*
 1287 *Biology*, 16: 1317-1337. doi:[10.1111/j.1365-2486.2009.02078.x](https://doi.org/10.1111/j.1365-2486.2009.02078.x)
 1288
 1289
 1290 Poulter, B., Frank, D., Ciais, P., Myneni, R.B., Andela, N., Bi, J., Broquet, G., Canadell, J.G.,
 1291 Chevallier, F., Liu, Y.Y., and Running, S.W.: Contribution of semi-arid ecosystems to interannual
 1292 variability of the global carbon cycle, *Nature*, 509, 600-603, <https://doi.org/10.1038/nature13376>,
 1293 2014.
 1294
 1295 Quetin, G., Bloom, A. A., Bowman, K. W., & Konings, A.: Carbon flux variability from a
 1296 relatively simple ecosystem model with assimilated data is consistent with terrestrial biosphere
 1297 model estimates. *Journal of Advances in Modeling Earth Systems*, 12,
 1298 e2019MS001889. <https://doi.org/10.1029/2019MS001889>, 2020
 1299
 1300 Randerson, J.T., Van Der Werf, G.R., Giglio, L., Collatz, G.J., and Kasibhatla, P.S.: Global Fire
 1301 Emissions Database, Version 4.1 (GFEDv4), ORNL DAAC, Oak Ridge, Tennessee,
 1302 USA, <https://doi.org/10.3334/ORNLDAAC/1293>, 2018.
 1303
 1304 Rienecker, M.M., Suarez, M.J., Gelaro, R., Todling, R., Bacmeister, J., Liu, E., Bosilovich, M.G.,
 1305 Schubert, S.D., Takacs, L., Kim, G.K., and Bloom, S.: MERRA: NASA's modern-era
 1306 retrospective analysis for research and applications, *J. Clim.*, 24, 3624-3648,
 1307 <https://doi.org/10.1175/JCLI-D-11-00015.1>, 2011.
 1308
 1309 Rödenbeck, C., Houweling, S., Gloor, M., and Heimann, M.: CO₂ flux history 1982–2001 inferred
 1310 from atmospheric data using a global inversion of atmospheric transport, *Atmos. Chem. Phys.*, 3,
 1311 1919–1964, <https://doi.org/10.5194/acp-3-1919-2003>, 2003.
 1312
 1313
 1314 Running, S.W., Baldocchi, D.D., Turner, D.P., Gower, S.T., Bakwin, P.S., and Hibbard, K.A.: A
 1315 global terrestrial monitoring network integrating tower fluxes, flask sampling, ecosystem
 1316 modeling and EOS satellite data, *Remote Sens. Environ.*, 70, 108-127,
 1317 [https://doi.org/10.1016/S0034-4257\(99\)00061-9](https://doi.org/10.1016/S0034-4257(99)00061-9), 1999.
 1318
 1319 Schuh, A.E., Jacobson, A.R., Basu, S., Weir, B., Baker, D., Bowman, K., Chevallier, F., Crowell,
 1320 S., Davis, K.J., Deng, F., and Denning, S.: Quantifying the impact of atmospheric transport
 1321 uncertainty on CO₂ surface flux estimates, *Global Biogeochem. Cy.*, 33, 484-500,
 1322 <https://doi.org/10.1029/2018GB006086>, 2019.
 1323
 1324 Sellers, P.J., Schimel, D.S., Moore, B., Liu, J., and Eldering, A.: Observing carbon cycle–climate
 1325 feedbacks from space, *PNAS*, 115, 7860-7868, <https://doi.org/10.1073/pnas.1716613115>, 2018.
 1326

1327 Stephens, B.B., Gurney, K. R., Tans, P. P., *et al.*: Weak northern and strong tropical land carbon
 1328 uptake from vertical profiles of atmospheric CO₂. *Science* **316**: 1732– 35,
 1329 doi:10.1126/science.1137004. 2007
 1330
 1331 Stephens, B., et al. 2017. ORCAS Airborne Oxygen Instrument. Version 1.0. UCAR/NCAR -
 1332 Earth Observing Laboratory. <https://doi.org/10.5065/D6N29VC6>.
 1333
 1334 Sweeney, C., Karion, A., Wolter, S., et al.: Seasonal climatology of CO₂ across North America
 1335 from aircraft measurements in the NOAA/ESRL Global Greenhouse Gas Reference Network. *J.*
 1336 *Geophys. Res. Atmos.*, 120, 5155– 5190. doi: [10.1002/2014JD022591](https://doi.org/10.1002/2014JD022591). 2015
 1337
 1338 Suntharalingam, P., Jacob, D.J., Palmer, P.I., Logan, J.A., Yantosca, R.M., Xiao, Y., Evans, M.J.,
 1339 Streets, D.G., Vay, S.L., and Sachse, G.W.: Improved quantification of Chinese carbon fluxes
 1340 using CO₂/CO correlations in Asian outflow, *J. Geophys. Res.: Atmos.*, 109, D18S18,
 1341 <https://doi.org/10.1029/2003JD004362>, 2004.
 1342
 1343 Tramontana, G., Jung, M., Schwalm, C. R., Ichii, K., Camps-Valls, G., Ráduly, B., Reichstein, M.,
 1344 Arain, M. A., Cescatti, A., Kiely, G., Merbold, L., Serrano-Ortiz, P., Sickert, S., Wolf, S., and
 1345 Papale, D.: Predicting carbon dioxide and energy fluxes across global FLUXNET sites with
 1346 regression algorithms, *Biogeosciences*, 13, 4291–4313, <https://doi.org/10.5194/bg-13-4291-2016>,
 1347 2016.
 1348 van der Laan-Luijkx et al, 2017, "The CarbonTracker Data Assimilation Shell (CTDAS) v1.0:
 1349 implementation and global carbon balance 2001-2015", [Geosci. Model Dev.](https://doi.org/10.5194/gmd-10-2785-2017), **10**, 2785-2800,
 1350
 1351 van der Werf, G. R., Randerson, J. T., Giglio, L., Gobron, N., and Dolman, A. J.: Climate
 1352 controls on the variability of fires in the tropics and subtropics, *Global Biogeochem. Cycles*, **22**,
 1353 GB3028, doi:[10.1029/2007GB003122](https://doi.org/10.1029/2007GB003122). 2008
 1354
 1355
 1356
 1357 Wofsy, S. C.: HIPER Pole-to-Pole Observations (HIPPO): Fine-grained, global-scale
 1358 measurements of climatically important atmospheric gases and aerosols, *Philos. Trans. R. Soc. A-*
 1359 *Math. Phys. Eng. Sci.*, 369, 2073– 2086, <https://doi.org/10.1098/rsta.2010.0313>, 2011.
 1360
 1361 Wofsy, S.C., Afshar, S., Allen, H.M., Apel, E., Asher, E.C., Barletta, B., Bent, J., Bian, H., Biggs,
 1362 B.C., Blake, D.R., and Blake, N.: ATom: Merged Atmospheric Chemistry, Trace Gases, and
 1363 Aerosols, ORNL DAAC, Oak Ridge, Tennessee,
 1364 USA, <https://doi.org/10.3334/ORNLDAAC/1581>, 2018.
 1365
 1366 Wunch, D., Toon, G.C., Blavier, J.F.L., Washenfelder, R.A., Notholt, J., Connor, B.J., Griffith,
 1367 D.W., Sherlock, V., and Wennberg, P.O.: The total carbon column observing network, *Philos.*
 1368 *Trans. R. Soc. A*, 369, 2087-2112, <https://doi.org/10.1098/rsta.2010.0240>, 2011.
 1369

1370 Yin, Y., Bowman, K., Bloom, A.A., and Worden, J.: Detection of fossil fuel emission trends in the
1371 presence of natural carbon cycle variability, *Environ. Res. Lett.*, 14, 084050,
1372 <https://doi.org/10.1088/1748-9326/ab2dd7>, 2019.
1373
1374 Zhu, C., Byrd, R.H., Lu, P., and Nocedal, J.: Algorithm 778: L-BFGS-B: Fortran subroutines for
1375 large-scale bound-constrained optimization, *ACM Trans. Math. Softw.*, 23, 550-560,
1376 <https://doi.org/10.1145/279232.279236>, 1997.
1377
1378
1379

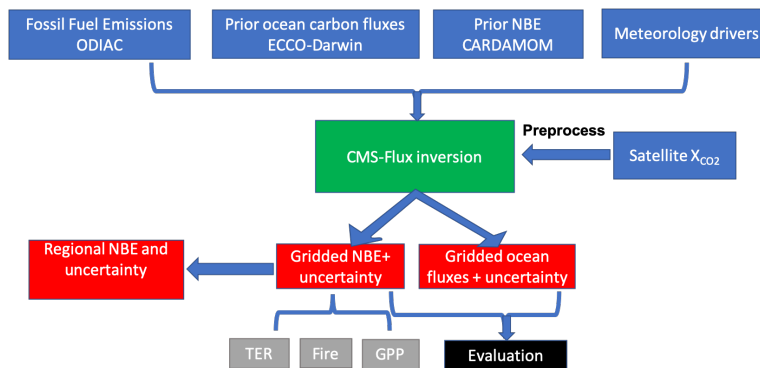


Figure: 1 Data flow diagram with the main processing steps to generate regional net biosphere change (NBE). TER: total ecosystem respiration; GPP: gross primary production. The green box is the inversion system. The blue boxes are the inputs for the inversion system. The red boxes are the data outputs from the system. The black box is the evaluation step, and the grey boxes are the future additions to the product.

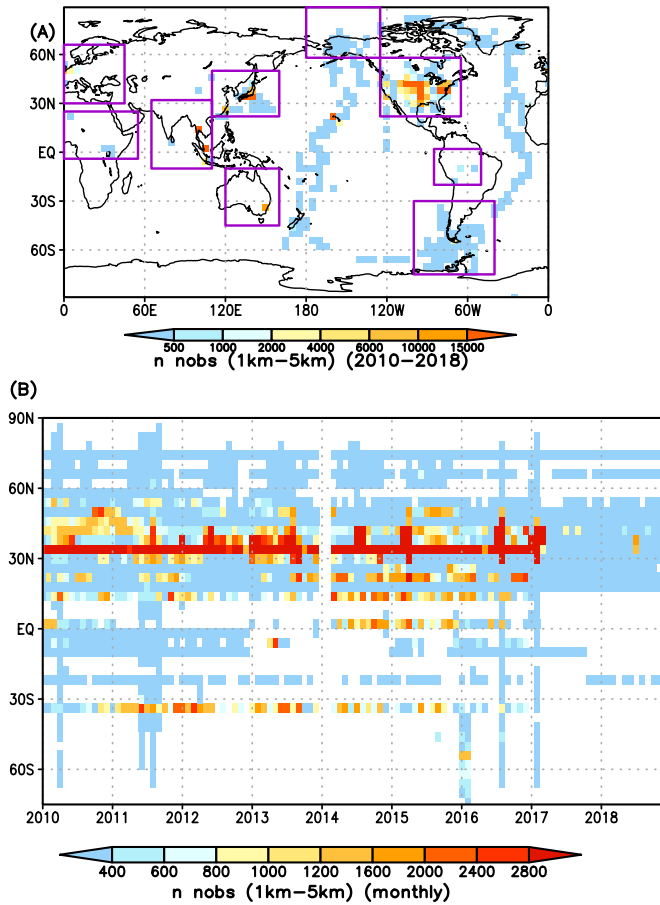


Figure: 2 The spatial and temporal distributions of aircraft observations used in evaluation of posterior NBE. (A) The total number of aircraft observations between 1–5 km between 2010–2018 at each $4^\circ \times 5^\circ$ grid point. The rectangle boxes show the range of the nine sub regions. (B) The total number of monthly aircraft observations at each longitude as a function of time.

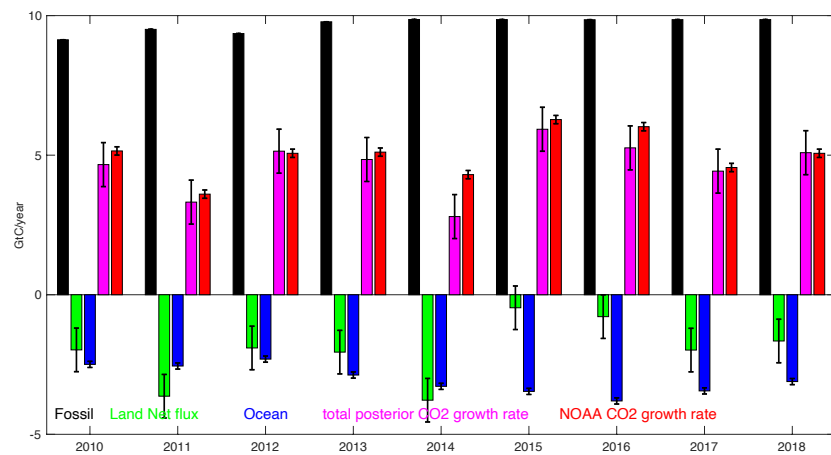
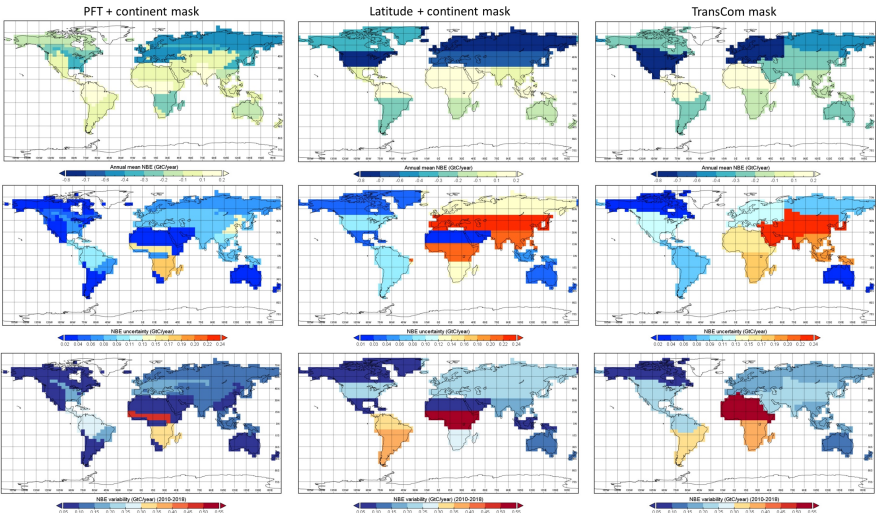


Figure: 4 Global flux estimation and uncertainties from 2010–2018 (black: fossil fuel; green: posterior land fluxes; blue: ocean fluxes; magenta: estimated CO₂ growth rate; red: the NOAA CO₂ growth rate).

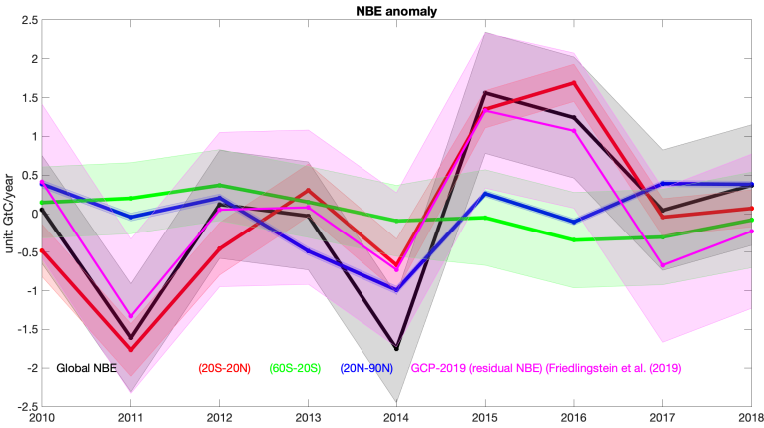
1417



1418
1419
1420
1421
1422
1423
1424

Figure: 5 Mean annual regional NBE (A, B, and C), uncertainty (D, E, and F), and variability between 2010–2018 (G, H, and I) with the three types of regional masks (Figure 3). The first column uses a region mask based on PFT and continents (RM1). The second column uses a region mask based latitude and continents (RM2), and the third column uses TransCom mask.

1425



1426

1427 **Figure: 6** The NBE interannual variability over the globe (black), the tropics (20°S–20°N),
1428 SH mid-latitudes (60°S–20°S), and NH mid-latitudes (20°N–9°0N). For reference, the
1429 residual net land carbon sink from GCB-2019 (Friedlingstein et al., 2019) and its uncertainty
1430 is also shown (magenta).

1431
1432
1433
1434

Deleted: GCP

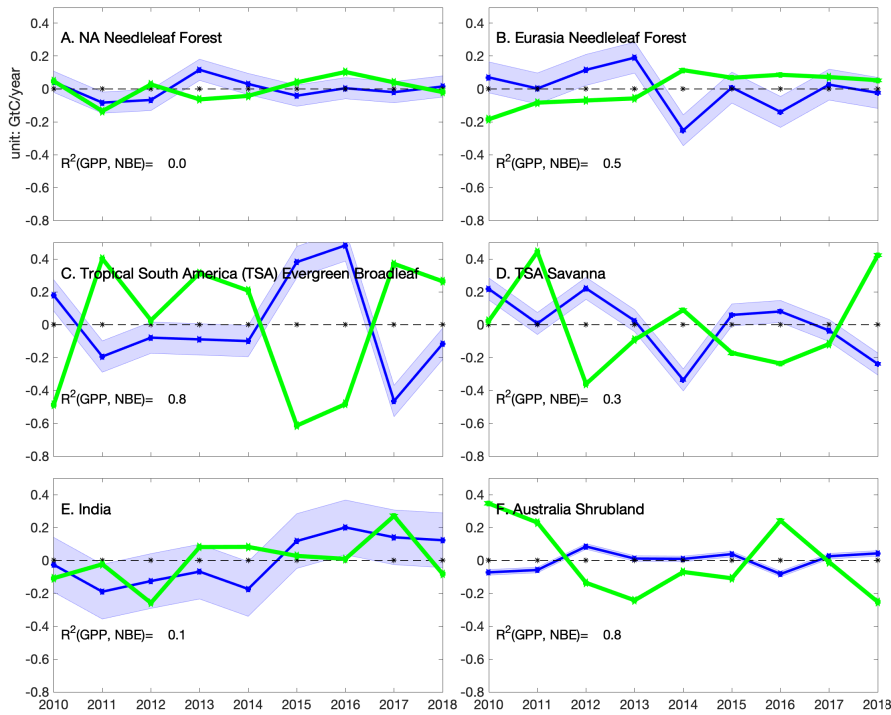


Figure: 7 The NBE interannual variability over six selected regions. Blue: annual NBE anomaly and its uncertainties. Green: annual GPP anomaly based on FLUXSAT.

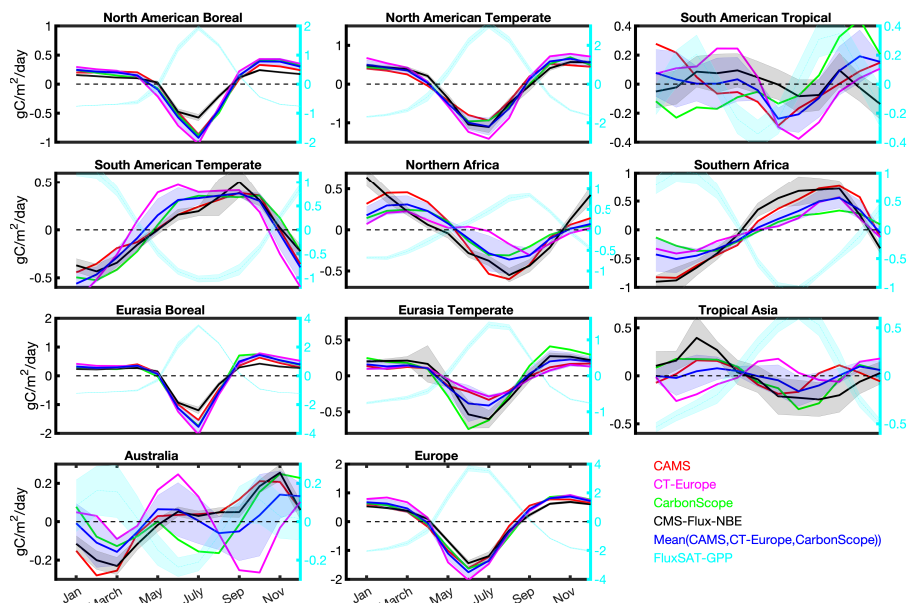


Figure: 8 The NBE climatological seasonality over TransCom regions. The seasonal cycle is calculated over 2010-2017 since CT-Europe only covers till 2017. Black: CMS-Flux-NBE and its uncertainty; blue shaded: mean NBE seasonality based on surface CO₂ inversion results from CAMS, CT-Europe, and Jena CarbonScope; red: CAMS; magenta: CT-Europe; green: Jena CarbonScope. The names of each region are shown on individual subplots.

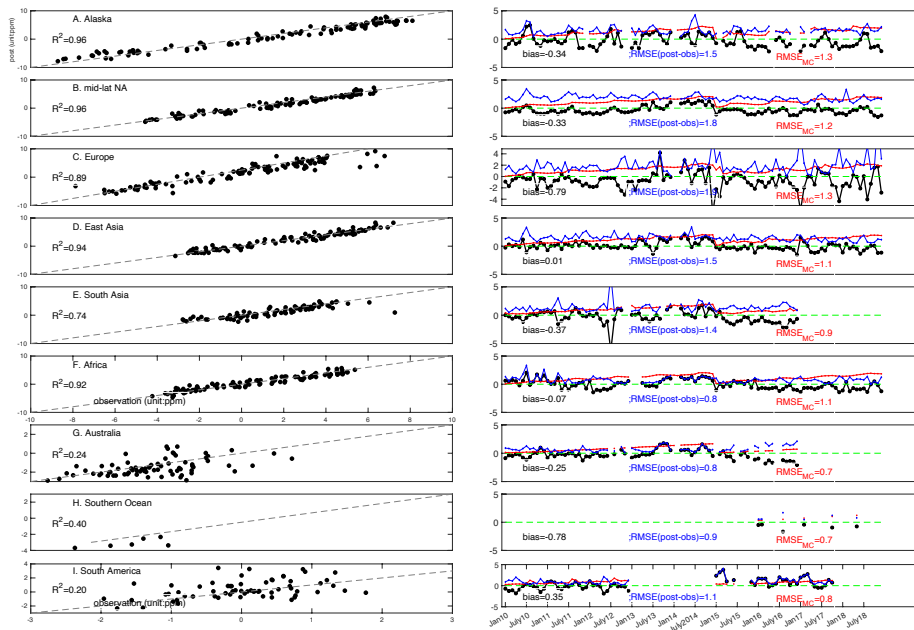
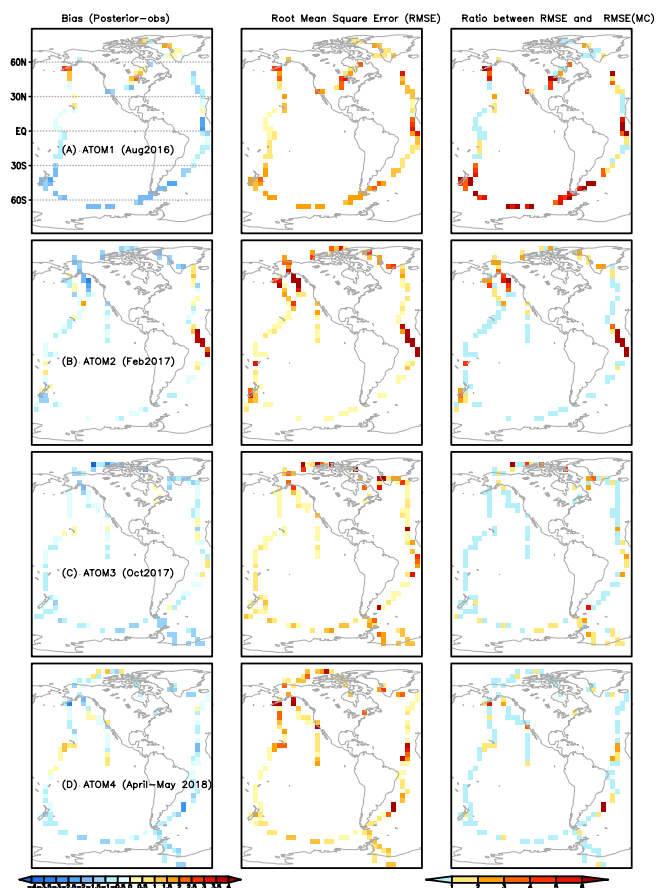


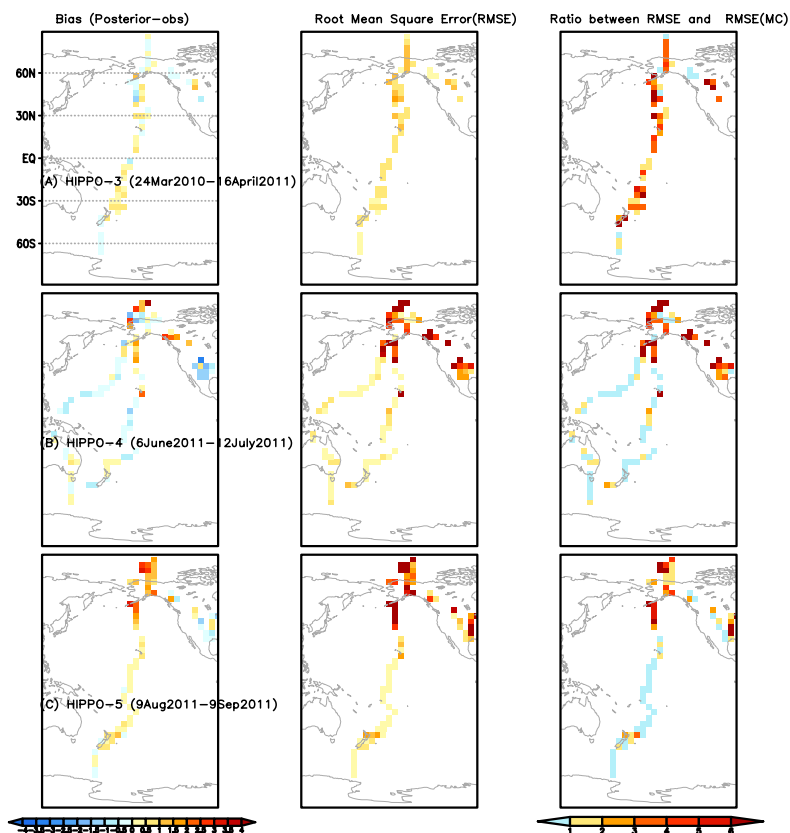
Figure: 9 Comparison between posterior CO₂ mole fraction and aircraft observations. Left panel: detrended posterior CO₂ (y-axis) vs. detrended aircraft CO₂ (x-axis) over nine regions. The dashed line is 1:1 line; right panel: black: the differences between posterior CO₂ and aircraft CO₂ as a function of time; blue: RMSE (unit: ppm); red: RMSE_{MC}.

1460
1461



1462

1463 **Figure: 10** Left column: the mean differences between posterior CO₂ and aircraft
1464 observations from ATOM 1–4 aircraft campaigns between 1–5 km (A–D). Middle column:
1465 the Root Mean Square Errors (RMSE) between aircraft observations and posterior CO₂
1466 between 1–5 km. The color bar is the same as the left column. Right column: the ratio
1467 between RMSE and RMSE_{MC} based on ensemble CO₂ from the Monte Carlo uncertainty
1468 estimation method.



1469

1470 **Figure: 11** Left column: the mean differences between posterior CO₂ and aircraft
 1471 observations from HIPPO 3-5 aircraft campaigns between 1–5 km (A–C) (unit: ppm). (unit:
 1472 ppm). The time frame of each campaign is in the figure. Middle column: the Root Mean
 1473 Square Errors (RMSE) between aircraft observations and posterior CO₂ between 1–5 km
 1474 (unit: ppm). The color bar is the same as the left column. Right column: the ratio between
 1475 RMSE and RMSE_{MC} based on ensemble CO₂ from the Monte Carlo method.

1476

1477

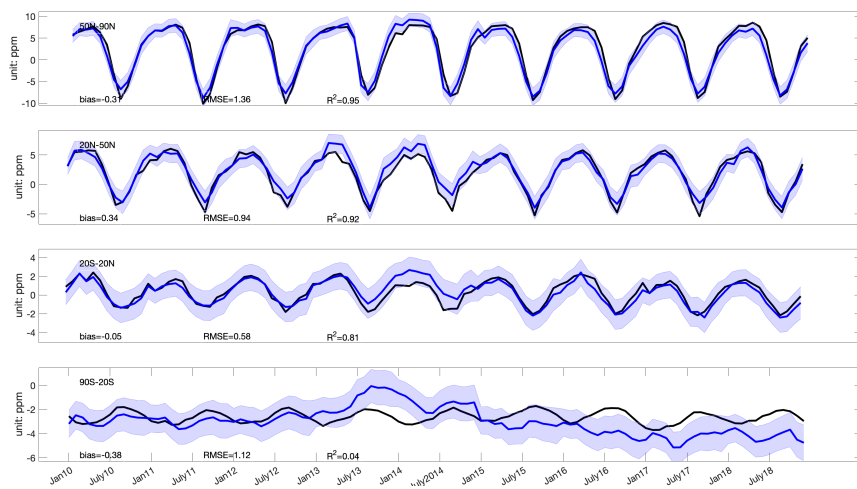


Figure: 12 Comparison between posterior CO₂ and the NOAA marine boundary layer (MBL) reference sites. Black: observations averaged over each latitude bands; blue and shaded area: posterior CO₂ and its uncertainty. The global mean CO₂ (<https://www.esrl.noaa.gov/gmd/ccgg/trends/global.html>) was subtracted from both the NOAA MBL reference and posterior CO₂ before the comparison.

1485
1486
1487
1488
1489
1490
1491

Table: 1 Configurations of the CMS-Flux atmospheric inversion system

	Model setup	Configuration	Reference
Inversion general setup	Spatial scale	Global	--
	Spatial resolution	4° latitude x 5° longitude	
	Time resolution	monthly	
	Minimizer of cost function	L-BFGS	Byrd et al., 1994; Zhu et al., 1997
	Control vector	Monthly net terrestrial biosphere fluxes and ocean fluxes	
Transport model	Model name	GEOS-Chem and its adjoint	Suntharalingam et al., 2004 Nassar et al., 2010 Henze et al., 2007
	Meteorological forcing	GEOS-5 (2010–2014) and GEOS-FP (2015–2019)	Rienecker et al., 2008

1492
1493

1494
1495

Table: 2 Description of the prior fluxes and assumed uncertainties in the inversion system

Prior fluxes	Terrestrial biosphere fluxes	Ocean fluxes	Fossil fuel emissions
Model name	CARDAMOM-v1	ECCO-Darwin	ODIAC 2018
Spatial resolution	4° x 5°	0.5°	1° x 1°
Frequency	3-hourly	3-hourly	hourly
Uncertainty	Estimated from CARDAMOM	100% same as Liu et al. (2017)	No uncertainty
References	Bloom et al., 2006; 2020	Brix et al, 2015; Carroll et al., 2020	Oda et al., 2016; 2018

1496

1497

1498

1499

1500

Table: 3 Description of observation and evaluation dataset. Data sources are listed in Table 7.

	Dataset name and version	References
Satellite X_{CO_2}	ACOS-GOSAT v7.3	O'Dell et al., (2012)
	OCO-2 v9	O'Dell et al., (2018)
Aircraft CO_2 observations	ObsPack OCO-2 MIP	CarbonTracker team (2019)
	HIPPO 3-5	Wofsy et al. (2011)
	ATom 1-4	Wofsy et al. (2018)
	INPE	Gatti et al., (2014)
	ORCAS	Stephens et al. (2017)
	ACT-America	Davis et al. (2018)
NOAA marine boundary layer (MBL) reference	NOAA MBL reference	Conway et al., 1994
GPP	FLUXSAT-GPP	Joiner et al., (2018)
Top-down NBE estimates constrained by surface CO_2	CarbonTracker-Europe	van der Laan-Luijkx et al. (2017) Peters et al., (2010) Peters et al. (2007)
	Jena CarbonScope s10oc v2020	Rödenbeck et al., 2003
	CAMS v18r1	Chevallier et al., 2005

1501

1502
1503
1504

Table: 4 Latitude and longitude ranges for seven sub regions.

Region	Alaska	Mid-lat NA	Europe	East Asia	South Asia
Longitude range	180°W–125° W	125°W–65°W	5°W–45°E	110°E–160°E	65°E–110°E
Latitude range	58°N–89°N	22°N–58°N	30°N–66°N	22°N–50°N	10°S–32°N
Region	Africa	South America	Australia	Southern Ocean	
Longitude range	5°W–55°E	95°W–50°W	120°E–160°E	110°W–40°E	
Latitude range	2°N–18°N	20°S–2°N	45°S–10°S	80°S–30°S	

1505
1506

1507 **Table: 5 List of the data products.**

Product	Spatial resolution	Temporal resolution when applicable	Data format	Sample data description in the text
Total fossil fuel, ocean, and land fluxes Climatology mean NBE, variability, and uncertainties	Global	Annual	csv	Figure 4 (section 4.1)
	PFT and continents based 28 regions	N/A	csv	Figure 5 (section 4.2)
	Geographic-based 13 regions		csv	
	TransCom regions		csv	
Hemispheric NBE and uncertainties	NH (20°N-90°N), tropics (20°S-20°N), and SH (60°S-20°S)	Annual	csv	Figure 6 (section 4.3)
NBE variability and uncertainties	PFT and continents based 28 regions	Annual	csv	Figure 7 (section 4.3)
	Geographic -based 13 regions		csv	
	TransCom regions		csv	
NBE seasonality and its uncertainties	PFT and continents based 28 regions	Monthly	csv	Figure 8 (section 4.4)
	Geographic -based 13 regions		csv	
	TransCom regions		csv	
Monthly NBE and uncertainties	PFT and continents based 28 regions	Monthly	csv	N/A
	Geographic -based 13 regions		csv	
	TransCom		csv	
Gridded posterior NBE, air-sea carbon exchanges, and uncertainties	4° (latitude) x 5° (longitude)	Monthly	NetCDF	N/A
Gridded prior NBE and air-sea carbon exchanges	4° (latitude) x 5° (longitude)	Monthly and 3-hourly	NetCDF	N/A
Gridded fossil fuel emissions	4° (latitude) x 5° (longitude)	Monthly mean and hourly	NetCDF	N/A
Region masks	PFT and continents based 28 regions	N/A	csv	Figure 3 (section 2.4)
	Geographic -based 13 regions			
	TransCom regions			

1508

1509

1510 **Table: 6 The nine-year mean regional annual fluxes, uncertainties, and variability. Regions**
1511 **are based on the mask shown in Figure 5A (Figure 5.csv). Unit: GtC/year**

Region name (Figure4.csv)	Mean NBE	Uncertainty	Variability
NA shrubland	-0.14	0.02	0.05
NA needleleaf forest	-0.22	0.04	0.06
NA deciduous forest	-0.2	0.04	0.07
NA crop natural vegetation	-0.41	0.06	0.18
NA grassland	-0.04	0.03	0.03
NA savannah	0.03	0.02	0.03
Tropical South America (SA) evergreen broadleaf	0.04	0.1	0.28
SA savannah	-0.09	0.06	0.18
SA cropland	-0.07	0.03	0.07
SA shrubland	-0.03	0.02	0.08
Eurasia shrubland savanna	-0.44	0.07	0.14
Eurasia needleleaf forest	-0.41	0.07	0.12
Europe cropland	-0.46	0.09	0.16
Eurasia grassland	0.02	0.08	0.13
Asia cropland	-0.37	0.13	0.08
India	0.14	0.09	0.14
Tropical Asia savanna	-0.12	0.11	0.08
Tropical Asia evergreen broadleaf	-0.09	0.09	0.12
Australia (Aus) savannah grassland	-0.11	0.02	0.09
Aus shrubland	-0.07	0.01	0.05
Aus cropland	-0.01	0.01	0.03
African (Afr) northern shrubland	0.04	0.02	0.03
Afr grassland	0.03	0.01	0.01
Afr northern savanna	0.54	0.15	0.49
Afr southern savanna	-0.27	0.18	0.33
Afr evergreen broadleaf	0.1	0.07	0.09
Afr southern shrubland	0.01	0.01	0.01
Afr desert	0.06	0.01	0.04

1512

1513

1514 **Table: 7 Lists of data sources used in producing and evaluating posterior NBE product.**

Data name	Data Source
ECCO-Darwin ocean fluxes	https://doi.org/10.25966/4v02-c391
CARDAMOM NBE and uncertainties	https://doi.org/10.25966/4v02-c391
ODIAC	http://db.eger.nies.go.jp/dataset/ODIAC/DL_odiac2019.html
GOSAT b7.3	https://oco2.gesdisc.eosdis.nasa.gov/data/GOSAT_TANSO_Level2/ACOS_L2S.7.3/
OCO-2 b9	https://disc.gsfc.nasa.gov/datasets?page=1&keywords=OCO-2
ObsPack	https://www.esrl.noaa.gov/gmd/ccgg/obspack/data.php
ATom 1-4	https://daac.ornl.gov/ATOM/guides/ATom_merge.html
HIPPO 3-5	https://www.eol.ucar.edu/field_projects/hippo
INPE	https://www.esrl.noaa.gov/gmd/ccgg/obspack/data.php?id=obspack_co2_1_INPE_RESTRICTED_v2.0_2018-11-13 and
FLUXSAT-GPP	https://gs614-avdc1-pz.gsfc.nasa.gov/pub/tmp/FluxSat_GPP/
NOAA MBL reference	https://www.esrl.noaa.gov/gmd/ccgg/mb1/index.html
CarbonTracker-Europe NBE	https://www.carbontracker.eu/download.shtml
Jena CarbonScope NBE	http://www.bgc-jena.mpg.de/CarboScope/?ID=s
CAMS NBE	https://apps.ecmwf.int/datasets/data/cams-ghg-inversions/?date_month_slider=2009-12,2018-12&param=co2&datatype=ra&version=v17r1&frequency=mm&quantity=surface_flux
Posterior NBE	https://doi.org/10.25966/4v02-c391

1515

1516

1517

1518

1519